

Characterization of Multi-Qubit Dark States in Waveguide Quantum Electrodynamics



Filip Hudek

University of Innsbruck
Faculty of Physics

Submitted to the Faculty of Mathematics, Computer Science, and Physics of the
University of Innsbruck



Master Thesis

submitted for the degree of
Master of Science

**Characterization of Multi-Qubit Dark States in Waveguide
Quantum Electrodynamics**

by

Filip Hudek, BSc
Matriculation Nr.: 01504584

Submission Date: August 20, 2024
Supervisors: Univ. Prof. Dr. Gerhard Kirchmair

Abstract

In the field of superconducting circuits, waveguide quantum electrodynamics (QED) has emerged as a promising platform for studying the interaction of quantum emitters with photons in an open environment [46]. In waveguide QED, superconducting qubits are coupled to engineered microwave waveguides. This setup facilitates the study of quantum optics in the microwave domain, enabling novel methods to control and manipulate the quantum states. The high degree of control and scalability offered by superconducting circuits makes them an ideal platform for investigating quantum many-body phenomena and advancing quantum computing technologies [9, 33]. By leveraging waveguide-mediated interactions, we can explore new regimes of quantum optics that are challenging to achieve with traditional atom-based systems [37, 60]. In this thesis, I outline a platform that implements waveguide-mediated interactions and interference effects in an ensemble of four transmon qubits to build and control decoherence-free subspaces for quantum computing. In this project, we have implemented an adiabatic elimination scheme realized through strong coupling to reduce leakage to higher excitation states [60]. As part of this thesis, I have also developed a coil tuning setup for better individual control of the flux-tunable transmons.

In the first part we characterized two transmon qubits forming collective states in the waveguide and demonstrated coherent control over the waveguide-decoupled dark state. Encoding the qubit in the dark state transition protects the information from radiative decay into the environment, significantly extending its lifetime. Then, using the developed flux-tuning schemes, the transmon effective emission frequency was adjusted so that the waveguide-mediated interactions form delocalized global states and demonstrated coherent control over them. We determined the characteristic decoherence times and proposed the implementation of a dark-state gate for future projects.

Contents

Abstract	iv
1 Introduction	11
2 Superconducting Quantum Circuits	13
2.1 The Quantum Harmonic Oscillator	13
2.2 The Josephson Junctions	15
2.2.1 The Transmon Qubit	17
2.2.2 Flux Tunability	19
3 Waveguide Quantum Electrodynamics	23
3.1 Waveguide Circuit Quantization	23
3.1.1 Waveguide-Qubit Coupling	25
3.1.2 Master Equation Formalism	27
3.2 Waveguide Mediated Interactions	30
3.2.1 Correlated Dissipation	30
3.2.2 Coherent Exchange Coupling	32
3.3 Direct Capacitive Coupling	33
3.4 Four Qubits in a Waveguide	34
4 Experimental Platform	35
4.1 Rectangular Waveguide	35
4.1.1 Sideport Driving	38
4.2 Transmon Qubits	39
4.2.1 Qubit Design Parameters	39
4.3 Coil Setup	41
4.4 Cryogenic Wiring	43
5 Characterisation of Multi-Qubit System in Rectangular Waveguide	47
5.1 Waveguide QED with Two Transmon Qubits	47
5.1.1 Flux Tuning	48
5.1.2 Power Saturation	50
5.1.3 Circle Fits	51
5.1.4 Avoided Crossing	52
5.1.5 Dark State Spectroscopy	53
5.1.6 Time Domain Characterization	55
5.2 Waveguide QED with Four Transmon Qubits	59
5.2.1 Rabi Oscillations on the Collective Dark State	59
5.2.2 Characteristic Decoherence Times of the Collective Dark State	60
6 Conclusions and Outlook	65
Bibliography	67

7 Acknowledgements

73

Introduction

Quantum physics emerged as a new field of study in the early 20th century, but only a few pioneers recognized its potential for technological innovation and societal transformation. By the 1940s, quantum physics had become a source of both hope and fear, as it enabled the development of nuclear energy and weapons. In the present era, quantum technologies have matured and diversified, finding applications in various domains such as cryptography [6, 48], communication [23, 40], computing [1, 42] or even quantum simulations [3, 15]. Some remarkable achievements have been made recently in field of quantum computing, such as solving problems that are virtually impossible for even the most powerful classical computers to handle [18, 61]. In these areas superconducting quantum circuits have become one of the most promising platforms [33]. The superconducting qubits have the advantage of being tunable and customizable, unlike natural atoms or ions. This allows for the exploration of novel regimes of light-matter interactions and quantum states.

Advances in quantum computation require a strong light-matter interaction between the photons and the quantum emitters. For this reason, most platforms incorporate a cavity or resonator to enhance this interaction and limit the modes for qubit decay. In superconducting quantum circuits, the protection and readout of quantum information are typically achieved by designing the qubit so that its resonance frequency is detuned from that of the resonator. In this regime, the cavity acts as a filter, protecting the qubit from noise around its resonance frequency, while the dispersive coupling of the qubit to the cavity allows for a non-demolition readout of the quantum state. Devices designed in this way operate in the dispersive limit, characterized by frequency detuning between the qubit and the cavity. However, there is another method for achieving quantum state protection in superconducting circuits while keeping the qubit resonant with propagating photons, thereby reaching strong coupling between quantum emitters and the light. Devices operating in the strong-coupling limit have qubits coupled to a specific channel much more strongly than to all the decoherence channels present in the system [59]. We use this approach in Waveguide Quantum Electrodynamics (QED), a platform that combines an open space environment and strong interactions, enabling state protection and coherent operations. Natural atoms, due to their small dipole moments, can only weakly couple to propagating photons [24]. In contrast artificial qubits, such as quantum dots or superconducting qubits, possess strong dipole moments, allowing for coupling efficiencies exceeding 99% [39]. The strong coupling of qubits to the propagating photons in the waveguide leads to waveguide-mediated interactions for multiple qubits on resonance, that form collective states.

In this thesis, we investigate one of these phenomena, the formation of multi-qubit dark states in Waveguide QED. This field studies the interactions of qubits with a continuum of

modes, which introduce a loss channel and limit the coherence time of quantum information. We will investigate how dark states can be created that exploit symmetry properties and interactions between four qubits. The decay time of the decoupled dark state is much longer compared to the single qubit decay time limited by the waveguide decay rate. Our research will enable the exploration of quantum many-body physics in waveguides and the implementation of quantum information protocols using subspaces that are immune to decoherence.

Superconducting Quantum Circuits

Following the footsteps of cavity quantum electrodynamics, which has allowed us to explore the interactions between atoms and electromagnetic fields, superconducting circuits have emerged as a valuable tool for studying the interactions between microwaves and electrical circuit elements. Recently, superconducting quantum circuits have become one of the most promising technologies for building quantum computers [9], being used as the platform to build these devices by some of the most prominent contributors to this field, such as IBM Quantum [27]. The LC harmonic oscillator is the most fundamental building block in circuit quantum electrodynamics [35], realized by arranging an inductor and a capacitor in a parallel configuration. There are many physical realizations of such a resonant circuit, which has become one of the most essential elements in quantum information technology with superconducting devices. In order to describe the electrical circuit in the quantum regime, we quantize the circuit in the first section. However, the harmonic nature of the LC harmonic oscillator prevents addressing individual transitions, as the energy levels are equally spaced. Addressing individual transitions is a necessity when defining a qubit. The Josephson junction is a device that can transform a harmonic oscillator into an anharmonic system, enabling selective addressing of individual transitions. In the field of circuit quantum electrodynamics (QED), the transmon qubit [34] is one of the most commonly used superconducting qubits. It is usually coupled to a microwave resonator or a waveguide to isolate it from the environment, while maintaining an access channel for coherent control. This coupling is essential for the proper functioning of the qubit in a quantum computer. In the final section we discuss a control of a transmon qubit using external magnetic flux to change to resonance frequency of the qubit.

2.1 The Quantum Harmonic Oscillator

To understand the structure and dynamics of superconducting qubits and waveguides, it is important to be familiar with the characteristics and properties of an LC resonator. The LC resonator circuit is a fundamental building block in superconducting quantum circuits. It is realized by arranging an inductor L and a capacitor C in parallel configuration, as shown in Figure 2.1 a). In such a circuit, the stored energy alternates between the magnetic field of the inductive element and the electrical field of the capacitor. In resonance, the magnetic and electric fields oscillate with frequency $\omega = 1/\sqrt{LC}$. The instantaneous time-dependent energy for each element of the circuit can be derived from the current I and the voltage V

$$E(t) = \int_0^t V(t')I(t')dt' \quad (2.1)$$

The circuit dynamics can be described by the Hamiltonian equation of motion, which we obtain from the given equation following the derivations in [13, 58]. We introduce the generalized branch fluxes $\Phi_b(t)$ and branch charges $Q_b(t)$, which are the energy variables of the circuit. They are related to the branch voltages $v_b(t')$ and branch currents $i_b(t')$ by the integrals:

$$\Phi_b(t) = \int_{-\infty}^t v_b(t')dt' \quad (2.2)$$

$$Q_b(t) = \int_{-\infty}^t i_b(t')dt'. \quad (2.3)$$

Here we assume the a vanishing voltage and vanishing current for the limit $t \rightarrow \infty$. The instantaneous energies at the components are then given by $E_C = \frac{1}{2C}(Q - Q_{\text{offset}})^2$ for the capacitor and $E_L = \frac{1}{2L}(\Phi - \Phi_{\text{offset}})^2$ for the inductor. The Hamiltonian, defined as the sum of energy contributions, can be formulated for LC resonator circuit without offset as [55]

$$H = E_C + E_L = \frac{Q^2}{2C} + \frac{\Phi^2}{2L}, \quad (2.4)$$

recognizing that the charge Q for this system resembles a 'kinetic energy' term and the flux Φ the 'potential energy'.

Since flux and charge are canonically conjugate variables, it is possible to apply canonical quantization $Q \leftrightarrow \hat{Q}$, $\Phi \leftrightarrow \hat{\Phi}$ to rewrite classical observables into the quantum formalism

$$H = \frac{\hat{Q}^2}{2C} + \frac{\hat{\Phi}^2}{2L}. \quad (2.5)$$

Here the operators $\hat{\Phi}$, \hat{Q} fulfill the commutation relation $[\hat{\Phi}, \hat{Q}] = i\hbar$, where \hbar is the reduced Plank constant. For determining the eigenstates of this Hamiltonian it is useful to define the lowering \hat{a}^\dagger and raising \hat{a} operators

$$\hat{\Phi} = \sqrt{\frac{\hbar}{2\omega_0 C}}(\hat{a} + \hat{a}^\dagger) \quad (2.6)$$

$$\hat{Q} = \sqrt{\frac{\hbar\omega_0 C}{2}}(\hat{a} - \hat{a}^\dagger). \quad (2.7)$$

The raising operator \hat{a} corresponds to adding the energy of a single photon with energy $\hbar\omega$ to the circuit and application of the lowering operator \hat{a}^\dagger consequently subtracts this energy from the system. These operators have to satisfy the commutation relation $[\hat{a}\hat{a}^\dagger] = 1$, if

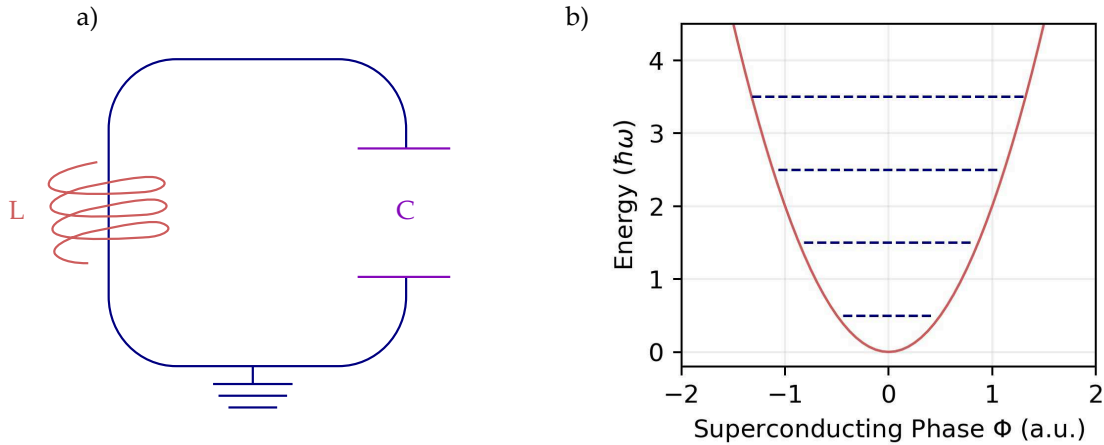


Figure 2.1: a) A circuit diagram of an LC resonator, consisting of a capacitor and an inductor connected in parallel. b) The energy spectrum of the quantum harmonic oscillator, which models the LC resonator as a single degree of freedom with equally spaced energy levels.

we substitute the relations 2.6 and 2.7 into the Hamiltonian 2.5 it is possible to simplify the equation to the form

$$\hat{H} = \hbar\omega \left(\hat{a}^\dagger \hat{a} + \frac{1}{2} \right). \quad (2.8)$$

In the discrete eigenbasis the expression $\hat{a}^\dagger \hat{a}$ is often abbreviated as the number operator $\hat{n} = \hat{a}^\dagger \hat{a}$ as it indicates the number of photons in the circuit. These coherent excitations are equidistantly spaced, separated by the energy $\hbar\omega$ as seen in the fig. 2.1.

It should be noted that at the ground state $\hat{n} = 0$, the energy of the circuit is not vanishing, instead takes a constant expectation value of $\hbar\omega/2$. This constant offset can also be seen in the prefactors of equations 2.6 and 2.7 and is referred to as 'zero point fluctuations' [13]. These play an important role for the experimental design of the experiments in superconducting qubits and will be discussed in the chapter 4 in further detail.

2.2 The Josephson Junctions

The fundamental characteristic of a quantum harmonic oscillator can be seen in its energy spectrum. The energy levels 2.1 are equally spaced in the potential well, separated by the energy difference $\hbar\omega$. This inherent harmonic behavior is making it challenging to address individual energy level transitions. This individual addressability is essential, when aiming to create a qubit - a coherent, controllable two-level system. To achieve this, we must incorporate a non-linear element into the LC oscillator circuit, disrupting the harmonicity. The non-linearity that is being used in superconducting quantum circuits is the Josephson Junction.

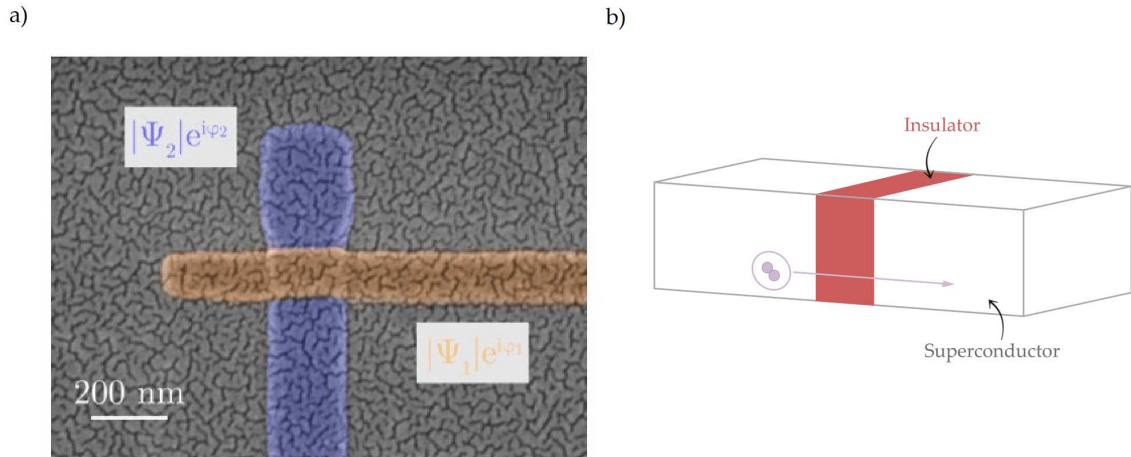


Figure 2.2: Josephson Junction. **a)** Picture taken on scanning electron microscope (SEM), a blue-colored superconductor is isolated from an orange superconductor by a thin insulating barrier at their intersection. In this picture, both superconductors are thin aluminum wires separated by aluminum oxide isolator. The rectangular overlap between them effectively creates a capacitance between the two metals. Picture from [60]. **b)** Schematic drawing of a Josephson junction consisting of two superconductors separated by a thin layer of insulator through which the cooper pairs tunnel through.

A Josephson junction is a fundamental circuit element in superconducting qubits. It consists of a thin insulating barrier, typically fabricated from aluminum oxide, that separates two superconducting layers of aluminum. Experimentally implemented as depicted in Fig. 2.2a), this structure exhibits a non-linear inductance, resulting in different level spacings between the excited energy levels [55].

When cooled below the critical temperature, Josephson junctions allow for a dissipationless current, referred to as the supercurrent I , to flow through the aluminum superconductor layer [56]. The spatial separation of superconducting layers by the barrier leads to distinct microscopic wavefunctions $\Psi_{1,2}$ with characteristic phase $\varphi_{1,2}$ and amplitude $|\Psi_{1,2}|$, describing the Cooper Pair condensates on each side of the tunnel barrier [5]. The phase difference across both sides of the barrier regulates the tunneling behavior of Cooper pairs through the barrier layer, resulting in the emergence of the supercurrent. The critical current I_c is a parameter that represents the maximum absolute current, beyond which Cooper pairs can no longer tunnel from one side of the junction to the other, while maintaining superconductivity. When subjected to stronger currents, the Josephson junction undergoes an abrupt transition to normal conduction behavior, resembling an ohmic resistor. This phenomenon was first observed by Brian D. Josephson in 1962 [30]. He described the relation between the supercurrent I and phase φ as

$$I = I_c \sin(\varphi). \quad (2.9)$$

The current I flowing across the tunnel barrier is clearly dependent on the phase φ . Additionally, Josephson introduced a relation describing the time evolution of the phase differ-

ence on both sides of the barrier, resulting in the appearance of a voltage drop V across the Josephson junction

$$V = \frac{\hbar}{2e} \frac{\partial \varphi}{\partial t}, \quad (2.10)$$

with the elementary charge of the electron e and the reduced Planck constant \hbar . Equation 2.10 allows us to relate the junction phase difference to the generalized flux [52] through $\Phi = \hbar\phi/2e$. The charge and flux are thus related through

$$\dot{q}(t) = I_c \sin\left(\frac{2\pi\Phi(t)}{\Phi_0}\right), \quad (2.11)$$

where the magnetic flux quantum $\Phi_0 = h/2e$ was used. The Josephson junction can be seen as a flux dependent inductor with an inductance given by

$$L(\phi) = -\frac{\Phi_0}{2\pi I_c \cos \varphi} = \frac{L_J}{\cos \varphi}, \quad (2.12)$$

where $L_J = \Phi_0/2\pi I_c$ is the characteristic inductance of the Josephson junction. The Josephson inductance L_J is describing a nonlinear inductor, as it depends on the cosine of phase difference φ across the junction.

Using the definition of charging energy $E_C = \frac{e^2}{2C_J}$, which describes the energy required to add each electron of the Cooper pair to the remaining Cooper pairs [56] and C_J the capacitance arising from the close proximity of the large metallic electrodes the Hamiltonian for the Josephson junction can be expressed as

$$\hat{H} = 4E_C(\hat{N})^2 - E_J \cos\left(\frac{\hat{\Phi}2\pi}{\Phi_0}\right) = 4E_C(\hat{N})^2 - E_J \cos(\hat{\varphi}), \quad (2.13)$$

where the normalized charge operator $\hat{N} = \frac{\hat{Q}}{2e}$ and phase operator $\hat{\varphi} = \frac{\hat{\Phi}2\pi}{\Phi_0}$ were used. The Hamiltonian 2.13 shows that the energy spectrum of a Josephson junction has an anharmonic behavior. The nonlinearity of the Josephson inductance introduces corrections to the energy spectrum, when expanding the cosine term. Consequently, the energy levels have unequal spacings, as depicted in Fig. 2.2b).

2.2.1 The Transmon Qubit

Replacing the linear inductor of a harmonic LC-oscillator with a Josephson junction alters the energy spectrum, as discussed in the chapter 2.2.

The different transition frequencies in the energy spectrum enable identifying a uniquely addressable two-level system within a multi-level anharmonic oscillator. Typically, we utilize the ground state and the first excited state as the computational basis states for qubit

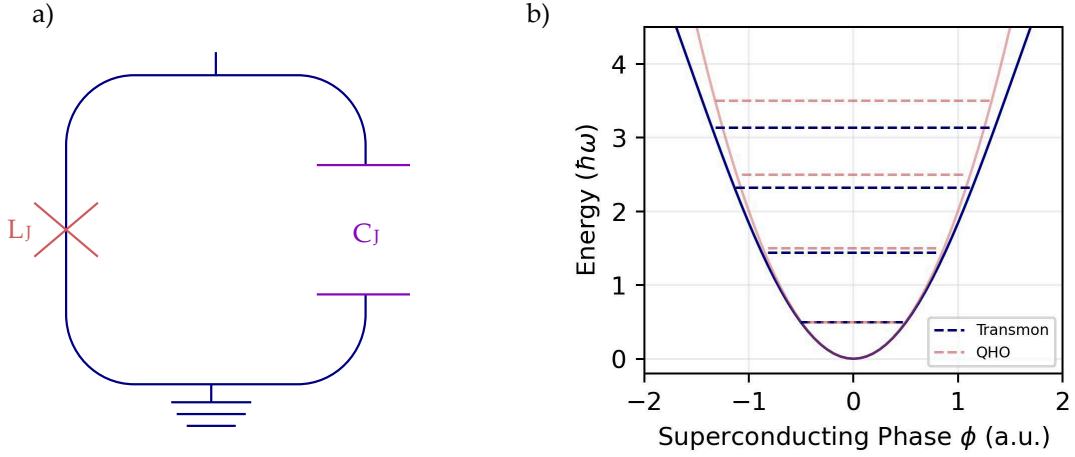


Figure 2.3: Transmon Qubit. a) A lumped circuit model of a transmon qubit, that consists of a capacitance in parallel with a Josephson junction, which is indicated by an orange cross symbol. b) Anharmonic energy spectrum of the eigenmodes of the LC resonator circuit with a Josephson junction replacing an inductor compared to quantum harmonic oscillator (QHO).

operations. A resonator circuit with Josephson inductance used instead of a linear inductive element is presented in Fig. 2.3. To distinguish the Josephson inductance from its linear counterpart, it is denoted by a cross symbol in the circuit diagram. This circuit can be modeled by the Hamiltonian

$$\hat{H} = \frac{(\hat{Q} - Q_g)^2}{2C_\Sigma} - E_J \cos\left(\frac{2\pi\hat{\Phi}}{\Phi_0}\right) = 4E_C(\hat{N} - N_g)^2 - E_J \cos\hat{\varphi}. \quad (2.14)$$

The Hamiltonian of the system given by equation 2.14 exhibits a strong dependence on the ratio E_J/E_C . By engineering the system such that $E_J \gg E_C$, we can suppress the effect of offset charges $N_g = \frac{Q_g}{2e}$ on the transition frequency, which are a significant source of dephasing [34]. To access this regime, a preferred approach is to reduce the charging energy E_C by shunting the junction with a large capacitor C_S . This circuit is commonly known as a transmon qubit [34], schematically depicted in Fig. 2.3 and the large shunt capacitors can be seen in Fig. 2.5. However, this regime also leads to a reduction in anharmonicity $\alpha = E_{12} - E_{01}$, which implies a smaller energy gap between levels. This can result in unwanted leakage from the ground state to higher excited states, especially when using fast pulses that are broad in frequency. Taking this into account, the Transmon typically operates in a regime where the ratio E_J/E_C is sufficiently large to render small charge noise negligible, while enabling fast manipulation of the qubit state relative to the decoherence time. When the inductive energy is large, we can expand the phase of the potential in the first terms

$$\cos(\hat{\varphi}) \approx \frac{1}{2}\hat{\varphi}^2 + \frac{1}{24}\hat{\varphi}^4. \quad (2.15)$$

This expansion results in a modified Hamiltonian

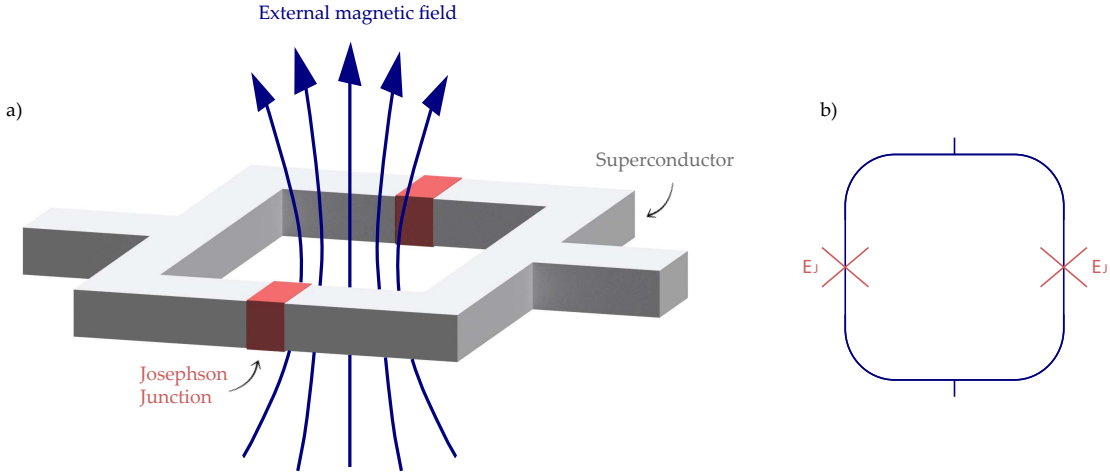


Figure 2.4: SQUID. a) Two Josephson junctions connected in parallel on a ring form a SQUID. Josephson junctions in SQUID configuration have an external flux-tunable E_J . b) Schematic circuit representation of a SQUID.

$$\hat{H} = 4E_c \hat{N}^2 - E_j \left(\frac{1}{2} \hat{\phi}^2 + \frac{1}{24} \hat{\phi}^4 \right). \quad (2.16)$$

To see the effect of the anharmonicity more clearly, we can quantize the Hamiltonian 2.16, which introduces the creation and annihilation operators [56]

$$\hat{H} \approx (\sqrt{8E_J E_C} - E_C) \hat{a}^\dagger \hat{a} - \frac{E_C}{2} \hat{a}^\dagger \hat{a}^\dagger \hat{a} \hat{a}. \quad (2.17)$$

The equation 2.17 shows that the fundamental qubit transition frequency is $\omega_{qb} = \sqrt{8E_J E_C} - E_C$, with a correction for each state by the anharmonicity E_C . As a consequence the energy level spacing becomes increasingly smaller for higher energy levels.

2.2.2 Flux Tunability

To manipulate the resonance frequency of the qubits externally, many circuits use a direct current superconducting quantum interference device, commonly known as dc-SQUID [35, 52], instead of a single Josephson junction. A dc-SQUID consists of two identical Josephson junctions connected in parallel on a ring, as shown in picture 2.4 and an external magnetic flux $\tilde{\Phi}$ flowing through the ring loop. The current passing through the SQUID is given by the sum of currents passing through each of the Josephson junctions.

$$I = I_{c,L} \sin(\phi_1) + I_{c,R} \sin(\phi_2) \quad (2.18)$$

where I_c is the critical current and ϕ the phase drop for each of the junctions respectively. For a symmetric SQUID loop with identical Josephson junctions the total current can be reformulated as [55]

$$I = I_c \left(\sin(\phi_1) + \sin \left(\phi_1 \frac{2\pi \tilde{\Phi}}{\Phi_0} \right) \right), \quad (2.19)$$

with the total flux through the loop $\Phi_B = BA$ and the flux quantum $\Phi_0 = h/2e$. For a given $\tilde{\Phi}$ there is a value of ϕ_1 that maximizes the total current I . The maximum value is the effective critical current of the SQUID, given by

$$I_{c,s}(\Phi_B) = 2I_c \left| \cos \left(\frac{\pi \tilde{\Phi}}{\Phi_0} \right) \right|. \quad (2.20)$$

The quantized critical current leads to an altered Josephson energy of the transmon [52]

$$E'_J(\tilde{\Phi}) = 2E_J \left| \cos \left(\frac{\tilde{\Phi}}{2} \right) \right|, \quad (2.21)$$

that is tunable with an external magnetic flux $\tilde{\Phi}$. Consequently, any changes in the effective Josephson energy E'_J lead to alterations in the resonance frequency

$$\omega_{01}(\tilde{\Phi}) = (\sqrt{8E'_J E_C} - E_C)/\hbar \quad (2.22)$$

of the qubit. For this effect, only the flux component that flows through the SQUID loop is of consideration.

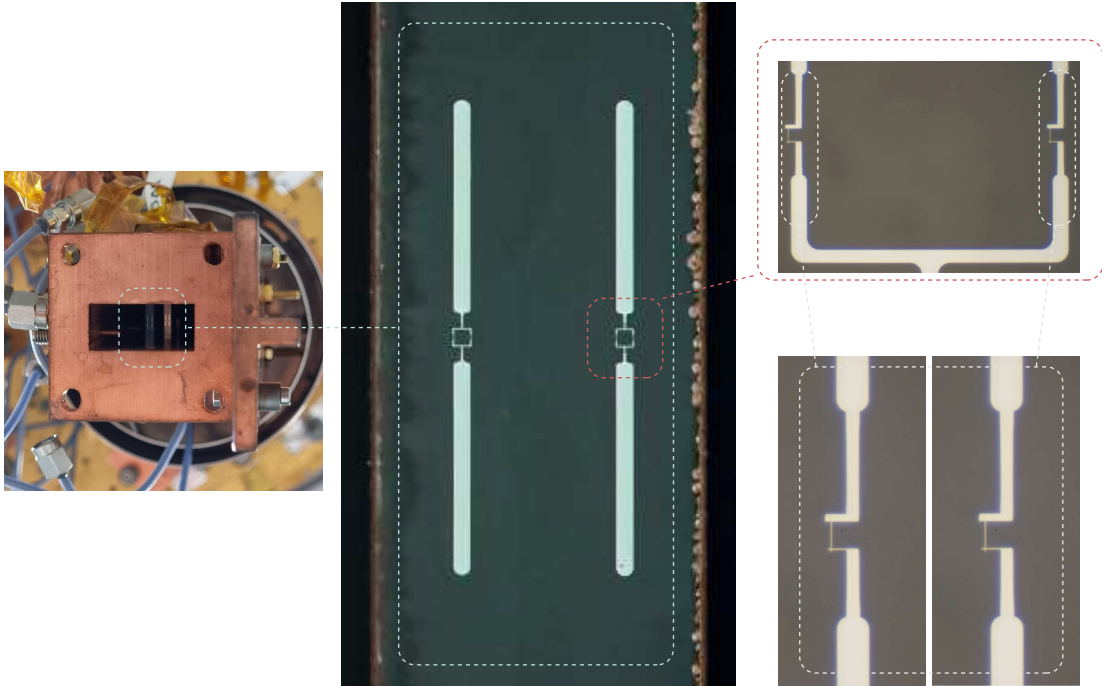


Figure 2.5: Transmon Qubits in SQUID Configuration. A picture of a half-open waveguide under an angle, such that both qubit sapphire chips are visible. A sapphire chip cut from a wafer by mechanical dicing saw is shown in the center, with zoom-in by an optical micrograph revealing the SQUID loop and individual junctions.

The SQUID loops used in this experiment have dimensions of $100\ \mu\text{m} \times 100\ \mu\text{m}$ and are spaced inside a pair $800\ \mu\text{m}$ center to center of the SQUID loops. Figure 2.5 shows the sapphire chip with a pair of transmon qubits including a zoom-in to the SQUID loop and the Josephson junction and a side view inside the waveguide with both qubit pairs visible.

Waveguide Quantum Electrodynamics

In the field of Waveguide Quantum Electrodynamics (QED) an artificial emitter is coupled to a one-dimensional channel that is propagating electromagnetic radiation to study the interaction between emitters and propagating mode continuum. In this chapter, we derive the mathematical description for a transmon qubit coupled to a rectangular waveguide.

3.1 Waveguide Circuit Quantization

To describe quantum properties of the system, we start by mathematically defining the waveguide. We model the continuous waveguide mode using the distributed elements approach. For the beginning, consider infinitesimal unit cells with a length of dx , each containing linear inductors Ldx and capacitors Cdx , as shown in Fig. 3.1. The derivations in this chapter closely follow quantization procedures from [22, 31, 58]. The voltage drop between positions x and $x+dx$ can be expressed as

$$V(x+dx, t) = V(x, t) - Ldx \frac{\partial I}{\partial t} \quad (3.1)$$

$$I(x+dx, t) = I(x, t) - Cdx \frac{\partial V}{\partial t}. \quad (3.2)$$

When we take the limit $dx \rightarrow 0$ and rearrange the equations, we arrive at the so-called “telegrapher equations”

$$\frac{\partial V(x, t)}{\partial x} = -L \frac{\partial I(x, t)}{\partial t} \quad (3.3)$$

$$\frac{\partial I(x, t)}{\partial x} = -C \frac{\partial V(x, t)}{\partial t}. \quad (3.4)$$

These equations describe the current flow and voltage across a transmission line or waveguide. Furthermore, we can define the generalized flux variable $\phi(x, t)$ in terms of voltage V along the waveguide [58]

$$\phi(x, t) = \int_{-\infty}^t V(x, \tau) d\tau, \quad (3.5)$$

which leads to the expression for voltage

$$V(x, t) = \dot{\phi}(x, t). \quad (3.6)$$

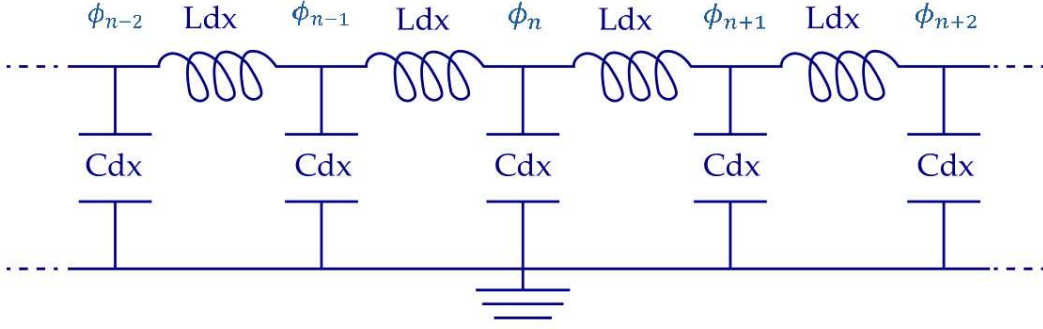


Figure 3.1: Circuit Diagram of a Waveguide. A circuit element model of a lossless transmission line (superconducting), characterized by inductance L and capacitance C per unit length. The flux nodes are denoted by $\Phi_n = \Phi(ndx, t)$.

Additionally, by considering the flux at each node $\Phi_n = \Phi(ndx, t)$ we can derive expressions for the inductive and capacitive energy density

$$E_C = \frac{C}{2} V(x, t)^2 = \frac{C}{2} \dot{\phi}(x, t)^2 \quad (3.7)$$

$$E_I = \frac{L}{2} I(x, t)^2 = \frac{L}{2} \left(\int \frac{dt}{L} \frac{\partial V}{\partial x} \right)^2 = \frac{1}{2L} \left(\frac{\partial \phi}{\partial x} \right)^2. \quad (3.8)$$

The Lagrangian is given by the difference between the kinetic energy T and the potential energy U , defined as $\mathcal{L} = T - U$. When considering ϕ as the position that leads to velocity $\dot{\phi}$, the Lagrangian can be expressed as

$$\mathcal{L} = E_C - E_I = \frac{C}{2} \dot{\phi}(x, t)^2 - \frac{1}{2L} \left(\frac{\partial \phi}{\partial x} \right)^2. \quad (3.9)$$

Differentiating with respect to velocity reveals the conjugate momentum of the flux node $\Phi(x, t)$, which corresponds to the charge density

$$q(x, t) = \frac{\partial \mathcal{L}}{\partial \dot{\phi}} = C \dot{\phi}(x, t) = CV(x, t). \quad (3.10)$$

Taking the Legendre transformation leads us to the Hamiltonian

$$H = \int_{-\infty}^{\infty} \left[\frac{1}{2} C q^2(x, t) + \frac{1}{2L} \left(\frac{\partial \Phi(x, t)}{\partial x} \right)^2 \right] dx, \quad (3.11)$$

where we have integrated over the infinite length of the waveguide. We can quantize the Hamiltonian using the standard quantization procedure by promoting the generalized coordinates to quantum operators, given that the charge and flux density are canonical conjugates: $q(x, t) = C \dot{\phi}(x, t)$. Additionally, we introduce the creation and annihilation

operators \hat{a}_k and \hat{a}_k^\dagger for a bosonic mode with wave vector k [47]. These operators fulfill the commutation relations

$$\left[\hat{\phi}(x, t), \hat{q}(x', t) \right] = i\hbar\delta(x - x') \quad (3.12)$$

$$\left[\hat{a}_k, \hat{a}_{k'}^\dagger \right] = \delta(k - k'), \quad (3.13)$$

from which can be seen that the relation for the same operators in different bosonic modes is zero and the operators do not commute for $x = x'$ and $k = k'$. Thus, enabling us to express the Hamiltonian in terms of the creation and annihilation operators

$$H = \sum_k \hbar\omega_k \left(\hat{a}_k \hat{a}_k^\dagger + \frac{1}{2} \right). \quad (3.14)$$

The Hamiltonian indicates that each mode k behaves like a linear quantum harmonic oscillator. The voltage and flux operators can be found to be [17, 58]

$$\hat{V}(x, t) = \frac{i}{\sqrt{2Cl}} \sum_k \sqrt{\hbar\omega_k} \left(\hat{a}_k e^{i(kx - \omega_k t)} - \hat{a}_k^\dagger e^{-i(kx - \omega_k t)} \right) \quad (3.15)$$

$$\hat{\Phi}(x, t) = \frac{1}{\sqrt{2Cl}} \sum_k \sqrt{\frac{\hbar}{\omega_k}} \left(\hat{a}_k e^{i(kx - \omega_k t)} + \hat{a}_k^\dagger e^{-i(kx - \omega_k t)} \right), \quad (3.16)$$

where length l was used as a periodic boundary condition, which we consider in limit $l \rightarrow \infty$ to create a continuum of modes along the waveguide propagation direction and arrive at the continuous form of voltage and flux

$$\hat{V}(x, t) = i \int \frac{d\omega}{\sqrt{2\pi}} \sqrt{\frac{\hbar\omega Z}{2}} \left(\hat{a}(\omega) e^{i(kx - \omega t)} - \hat{a}^\dagger(\omega) e^{-i(kx - \omega t)} \right) \quad (3.17)$$

$$\hat{\Phi}(x, t) = \int \frac{d\omega}{\sqrt{2\pi}} \sqrt{\frac{\hbar Z}{2\omega}} \left(\hat{a}(\omega) e^{i(kx - \omega t)} + \hat{a}^\dagger(\omega) e^{-i(kx - \omega t)} \right), \quad (3.18)$$

with the characteristic line impedance $Z = \sqrt{L/C}$.

3.1.1 Waveguide-Qubit Coupling

In this section, we develop the Hamiltonian description for a qubit coupled to an infinite waveguide, a circuit illustrated in Fig. 3.2. The transmon qubit, which has a physical size significantly smaller than the waveguide propagating modes, can be represented as a lumped circuit element capacitively coupled to a single node in the circuit.

The discrete Lagrangian for this circuit can be expressed as described in references [47, 54] as

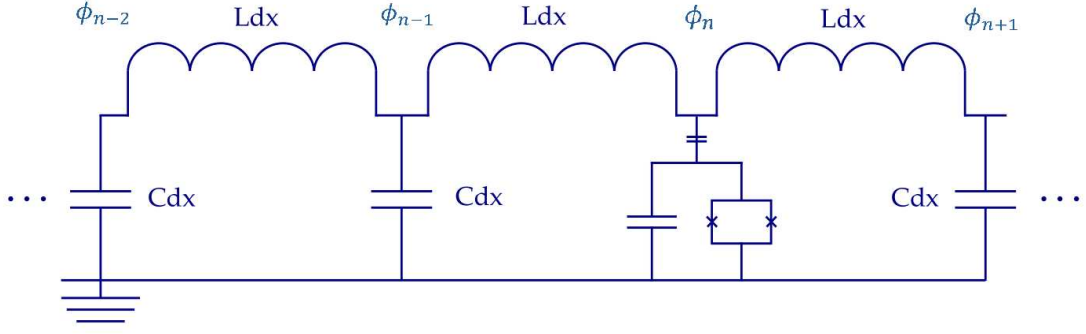


Figure 3.2: Circuit Diagram: Transmon Qubit Coupled to a Waveguide.

A lossless waveguide with flux nodes that are denoted as $\Phi_n = \Phi(ndx, t)$. Transmon qubit is capacitively coupled to the waveguide and is thus interacting with propagating microwave modes.

$$\begin{aligned} \mathcal{L} = \sum_n \frac{Cdx}{2} \dot{\Phi}_n(t)^2 - \frac{(\Phi_{n+1}(t) - \Phi_n(t))^2}{2Ldx} + \frac{C_q}{2} \dot{\Phi}_q(t)^2 \\ + E_J \left(\Phi_{ext} \cos \left(\frac{2e\Phi_q}{\hbar} \right) \right) + \frac{C_c}{2} (\dot{\Phi}_0(t) - \dot{\Phi}_q(t))^2, \end{aligned} \quad (3.19)$$

where we account for all the waveguide nodes $\Phi_n(t) = \Phi(ndx, t)$. The flux node Φ_q contains a qubit with flux-tunable $E_J(\Phi_{ext})$, located at the position of the waveguide $x = 0$. The conjugate variable of the flux is, analogously to 3.10, the charge

$$Q_q(t) = \frac{\partial \mathcal{L}}{\partial \dot{\Phi}_q} = C_q \dot{\Phi}_q(t) + C_c (\dot{\Phi}_0(t) - \dot{\Phi}_q(t)). \quad (3.20)$$

The capacitance C_c facilitates coupling to the waveguide and also contributes to the overall transmon capacitance, along with the junction capacitance C_q . Assuming that the capacitance of the waveguide is much larger than the other capacitive contributions ($C_w \gg C_c, C_q$), the qubit capacitances act as a small perturbation in the waveguide. The canonical quantization of the waveguide charge \hat{q} , flux $\hat{\Phi}$, and the qubit charge \hat{Q} and flux $\hat{\Phi}_q$ yields the Hamiltonian

$$\begin{aligned} \hat{H} = \int_{-\infty}^{\infty} \frac{\hat{q}(x, t)^2}{2C} + \frac{1}{2L} \left(\frac{\partial \hat{\Phi}(x, t)}{\partial x} \right)^2 dx + \frac{\hat{Q}_q(t)^2}{2(C_c + C_q)} \\ - E_J \cos \left(\frac{2e\hat{\Phi}_q}{\hbar} \right) + \frac{C_c}{C'} \hat{q}(0, t) \hat{Q}_q(t). \end{aligned} \quad (3.21)$$

With the total capacitance given by $C' = C_q + C_c C$, the capacitive coupling of the transmon qubit to waveguide exhibits a “charge-like” interaction. Quantized charge $\hat{q}(x, t) =$

$C\hat{V}(x, t)$ and flux $\hat{\Phi}(x, t)$ have continuous forms [17], analogous to 3.17 and 3.18, expressed with creation and annihilation operators as

$$\hat{V}(x, t) = iC \int \frac{d\omega}{\sqrt{2\pi}} \sqrt{\frac{\hbar\omega Z}{2}} \left(\hat{a}(\omega) e^{i(kx - \omega t)} - \hat{a}^\dagger(\omega) e^{-i(kx - \omega t)} \right) \quad (3.22)$$

$$\hat{\Phi}(x, t) = \int \frac{d\omega}{\sqrt{2\pi}} \sqrt{\frac{\hbar Z}{2\omega}} \left(\hat{a}(\omega) e^{i(kx - \omega t)} + \hat{a}^\dagger(\omega) e^{-i(kx - \omega t)} \right). \quad (3.23)$$

To describe energy in the system, we used inductances and capacitances associated with the waveguide and the transmon qubit. While the Hamiltonian fully characterizes the system, we used second quantization for a quantum mechanical perspective, expressing flux and charge operators via creation and annihilation operators. This approach is particularly useful for the transmon, when focusing on its two lowest energy states.

3.1.2 Master Equation Formalism

After deriving the interaction between a single transmon qubit and a waveguide, we can extend this approach to multiple qubits [37, 47]. We start by rewriting the Hamiltonian from equation 3.21 using second quantization, substituting equations 3.22 and 3.23. The Hamiltonian describing the waveguide propagating modes reads

$$\hat{H}_{EM} = \int_0^\infty d\omega \hbar\omega (\hat{a}_r^\dagger(\omega) \hat{a}_r(\omega) + \hat{a}_l^\dagger(\omega) \hat{a}_l(\omega)), \quad (3.24)$$

where $\hat{a}_{r(l)}(\omega)$ represents the right (left) waveguide propagating field modes with positive (negative) wave vector $k = \pm 2\pi/\lambda$. The electromagnetic modes propagating through the waveguide are described as right- and left-moving photons that are created by $\hat{a}_{r(l)}^\dagger(\omega)$ and annihilated by $\hat{a}_{r(l)}(\omega)$ at frequency ω . We approximate the transmon qubits as two-level systems, meaning it is sufficient to describe the j^{th} qubit charge operator as the σ_j^x Pauli matrix. We furthermore neglect direct capacitive coupling between qubits, leading to a simplified Hamiltonian description

$$\hat{H}_Q = \hbar \sum_{j=1}^N \omega_j \hat{\sigma}_j^+ \hat{\sigma}_j^-. \quad (3.25)$$

Here $\hat{\sigma}^+$ is the Pauli raising operator and $\hat{\sigma}^-$ is the Pauli lowering operator. Considering only the ground and excited states, qubit has a bare fundamental transition frequency ω . The coupling between the electrical dipole of qubits and the waveguide photons is expressed in the interaction Hamiltonian

$$\begin{aligned} \hat{H}_I = \sum_{j=1}^N i\hbar g_j \int_0^\infty d\omega \sqrt{\omega} \left[\hat{a}_l^\dagger(\omega) e^{i\omega x_j/v} - \hat{a}_l(\omega) e^{-i\omega x_j/v} \right. \\ \left. + \hat{a}_r^\dagger(\omega) e^{-i\omega x_j/v} - \hat{a}_r(\omega) e^{i\omega x_j/v} \right] \sigma_j^x, \end{aligned} \quad (3.26)$$

where x_j is the position of the j^{th} qubit, speed of light in the waveguide is denoted as v and the qubit charge operator was approximated as $\sigma_j^x = \sigma_j^+ + \sigma_j^-$. The dimensionless coupling rate g_j between the j^{th} qubit and the waveguide is

$$g_j = \sqrt{\frac{e^2 C}{2\hbar\pi v \left(\frac{C'_j}{C_{e,j}}\right)^2}} \left(\frac{E_J}{EC}\right)^{\frac{1}{4}} \quad (3.27)$$

The Hamiltonian, comprising the waveguide field part \hat{H}_{EM} , qubit part \hat{H}_Q and interaction part \hat{H}_I , fully describes the system within the stated approximations. However, due to the continuum of field modes in the waveguide, performing calculations is challenging. Fortunately, we can insert the Hamiltonian into a master equation for the qubit density operator $\hat{\rho}$, which treats the degrees of freedom of the waveguide as a dissipative bath coupled to the qubits [10, 26, 37, 39]. This approach only tracks the dynamics of the qubits and their mutual interactions via the waveguide and can be expressed as

$$\frac{d\hat{\rho}}{dt} = -i \left[\frac{\hat{H}_Q}{\hbar} + \sum_j \alpha_j(t) \hat{\sigma}_j^x + \sum_{j,k} \tilde{J}_{j,k} \hat{\sigma}_k^+ \hat{\sigma}_j^-, \hat{\rho} \right] + \sum_{j,k} \gamma_{j,k} \left(\hat{\sigma}_j^- \hat{\rho} \hat{\sigma}_k^+ - \frac{1}{2} \{ \hat{\sigma}_k^+ \hat{\sigma}_j^-, \hat{\rho} \} \right). \quad (3.28)$$

Here, the first part of the equation in the square brackets can be considered the "coherent part." The term \hat{H}_Q represents the qubit Hamiltonian as defined in equation 3.25. The second term describes the coherent time-dependent drive $\alpha(t)$ that the qubits experience from the waveguide propagating photons. We assume photons traveling from left and acting on qubits located at position $x_j = t_j v$ as

$$\alpha_j(t) = \frac{\Omega_j}{2} \sin(\omega_d(t + t_j)), \quad (3.29)$$

where Ω_j is the drive amplitude with frequency ω_d as experienced by the qubit at the position j . The last term of eq. 3.28 describes the two-qubit exchange coupling $\tilde{J}_{j,k}$, and together with the rest of the master equation, which can be considered the "dissipative part," it characterizes the waveguide-mediated interactions [37, 57, 60]. These interactions occur as photons travel in the waveguide from the qubit at position j to the qubit at position k . The coefficient $\gamma_{j,k}$ represents the correlated decay between the qubits at these two sites. Assuming resonant qubits and the time $t_{j,k} = |t_j - t_k|$ that photons take to travel from j to k , the coefficients of waveguide mediated interactions are given by

$$\tilde{J}_{j,k} = 2\pi g_j g_k \omega_j \sin(\omega_j t_{j,k}), \quad (3.30)$$

$$\gamma_{j,k} = 4\pi g_j g_k \omega_j \cos(\omega_j t_{j,k}). \quad (3.31)$$

The form of these coefficients implies that qubit spacing plays a crucial role in waveguide-mediated interactions. For two qubits separated by an integer multiple of $\lambda/2$, the correlated decay $\gamma_{j,k}$ is maximized and the coherent exchange interaction $\tilde{J}_{j,k}$ is absent. Conversely, when the qubits at positions j and k are spaced apart by an odd integer multiple of $\lambda/4$, the $\tilde{J}_{j,k}$ is maximized and the correlated decay $\gamma_{j,k}$ is zero.

To further simplify the problem, we can assume that $\alpha(t)$ is the only coherent drive with photons propagating from left to right. This assumption allows us to eliminate time dependence of the Hamiltonian by transitioning to the rotating frame at the drive frequency. The rotating wave approximation (RWA) removes the rapidly oscillating terms, resulting in the Hamiltonian taking the form of

$$\hat{H}_{\text{RWA}} = \hbar \sum_{j=1}^N \Delta_j \hat{\sigma}_j^+ \hat{\sigma}_j^- + \hbar \sum_{j=1}^N \left(\frac{\Omega_{l,j}}{2} \hat{\sigma}_j^+ + h.c. \right) + \hbar \sum_{j \neq k}^N \tilde{J}_{j,k} \hat{\sigma}_j^+ \hat{\sigma}_k^-, \quad (3.32)$$

with $\Delta_j = \omega_j - \omega_d$ the detuning of the qubit drive. In this model, we have so far only considered the qubit decay into the waveguide and have not accounted for other decay channels, such as the non-radiative spontaneous decay rate γ_{nr} or the pure dephasing rate of the qubit γ_ϕ . It should be noted that the ‘‘non-radiative’’ decay channel is a physically radiative process accounting for all intrinsic relaxation rates, just not in the mode of interest. We account for these decay channels by replacing the waveguide coupling rate in the master equation with the effective decay rate $\Gamma = \gamma_{nr} + \gamma_\phi$. While we account for these decay channels, we operate in regime where the coupling to the waveguide is much larger than all the decoherence channels $\gamma_r \gg \Gamma$, known as the strong coupling regime. Incorporating all decay channels we can rewrite the master equation as

$$\frac{d\hat{\rho}}{dt} = -\frac{i}{\hbar} [\hat{H}_{\text{RWA}}, \hat{\rho}] + \sum_{j,k}^N \gamma'_{j,k} \left(\hat{\sigma}_j^- \hat{\rho} \hat{\sigma}_k^+ - \frac{1}{2} \hat{\sigma}_k^+ \hat{\sigma}_j^-, \hat{\rho} \right) + \sum_{j=1}^N \frac{\gamma_{\phi,j}}{2} \left(\hat{\sigma}_j^z \hat{\rho} \hat{\sigma}_j^z - \hat{\rho} \right). \quad (3.33)$$

This expression can be solved analytically in steady state $\dot{\hat{\rho}} = 0$ and allows to express the density matrix in terms of the drive amplitude and qubit decoherence rates. In the experiment however, we measure the photons traveling through the waveguide, that can be described with the input-output theory [37]. Photons propagating from left to right in the waveguide can be described as [14, 19, 44]

$$\hat{a}_{out} = \hat{a}_{in} - i\sqrt{\frac{\gamma_r}{2}} \hat{\sigma}^-. \quad (3.34)$$

The expectation value of the annihilation operator \hat{a} is directly related to the drive amplitude, which allows to define the complex waveguide transmission parameter S_{21} as ratio between the input and output fields [37]

$$S_{21}(\omega) = \frac{\langle \hat{a}_{out} \rangle}{\langle \hat{a}_{in} \rangle} = 1 - \frac{\gamma_r}{2\Gamma} \frac{1 - \frac{i\delta\omega}{\Gamma}}{1 + \left(\frac{\delta\omega}{\Gamma}\right)^2 + \frac{\Omega^2}{(\gamma_r + \gamma_{nr})\Gamma}}, \quad (3.35)$$

with the total qubit decoherence rate Γ consisting of waveguide radiative decay γ_r and qubit intrinsic ‘‘non-radiative’’ decay γ_{nr} . We analyze the intrinsic qubit properties with the circle-fit routine for developed originally for resonators coupled to a transmission line in notch-configuration [32, 51]. With this procedure the impedance mismatches and the environment are taken into account. We fit to the measurement data the complex transmission parameter expressed in terms of the quality factors

$$S_{21}(f) = ae^{i\alpha} e^{-2\pi if\tau} \left[1 - \frac{(Q_l/Q_c)e^{i\phi}}{1 + 2iQ_i(f/f_r - 1)} \right]. \quad (3.36)$$

Here the Q_l describes the loaded, Q_c the coupling and Q_i the internal quality factor. The resonance frequency of the transition is denoted f_r and probe frequency f . The fit considers also the effect of impedance mismatch in parameter ϕ and environment in amplitude parameter a , phase shift α and electronic delay τ . The quality factors are related to the decoherence rates [11, 12] obtained from the eq. 3.35 as

$$Q_l = \frac{\omega_{01}}{2\Gamma} \quad Q_c = \frac{\omega_{01}}{\gamma_r} \quad Q_i = \frac{\omega_{01}}{2\gamma_{nr}}. \quad (3.37)$$

3.2 Waveguide Mediated Interactions

In the theoretical derivations so far, we primarily considered the physics of a single qubit coupled to the waveguide. Now, we aim to discuss waveguide-mediated interactions that occur when multiple qubits couple to the photons propagating through the waveguide. Specifically, we will examine how the phase acquired by a photon traveling between two qubits plays a crucial role in the nature of the interaction between them. From the counter-periodic behavior of eqs. 3.30 and 3.31, it is evident that by tuning either the physical distance λ between the qubits, the photon velocity v or the qubit emission frequency ω_q , we can switch between different types of interactions between the qubits [37, 44]. We utilize the flux-tunability of the Josephson junctions in a SQUID configuration to experimentally tune the resonance frequency of the qubit, thus altering the effective emission wavelength λ .

3.2.1 Correlated Dissipation

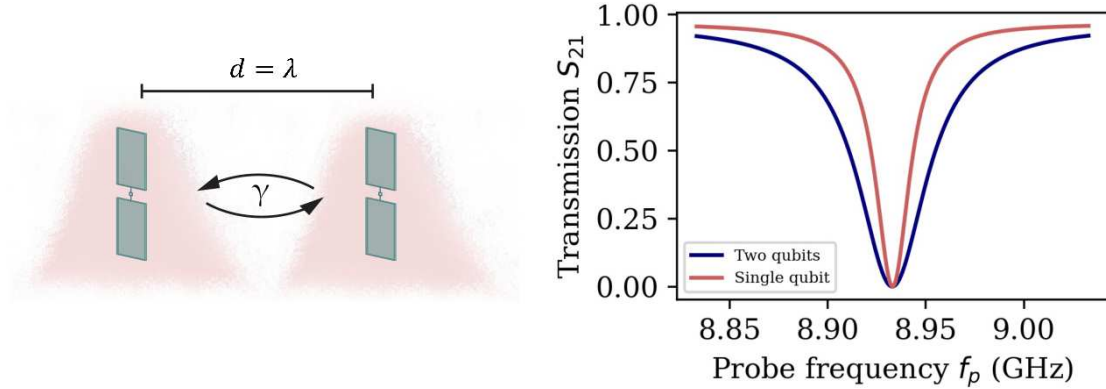


Figure 3.3: Two qubits at effective separation $d = \lambda$ are tuned to resonance, which leads to formation of new eigenstates. Eigenstate corresponding to the superradiant transition experiences broadening of the linewidth, while the subradiant transition is absent from the transmission spectrum and cannot be driven.

If we consider the case of two resonant qubits, $\omega_1 = \omega_2 = \omega_q$, effectively spaced by a distance $d = \lambda$ with respect to the qubit frequency ω_q , the correlated dissipation $\gamma_{j,k}$ will

be maximized while there will be no coherent exchange coupling $\tilde{J}_{j,k}$ between the qubits j, k . We can further assume that there is no drive while temporarily ignoring all decoherence channels unrelated to the waveguide. Under these conditions, the master equation will depend only on the dissipators and will take the form [37]

$$\frac{d\hat{\rho}}{dt} = \sum_{\mu=B,D} \Gamma_{\mu} \mathcal{D} \left[\hat{\sigma}_{\mu}^{-} \right] \hat{\rho}, \quad (3.38)$$

where $\mathcal{D} \left[\hat{\sigma}_{\mu}^{-} \right] \hat{\rho} = \hat{\sigma}_{\mu}^{-} \hat{\rho} \hat{\sigma}_{\mu}^{+} - \{ \hat{\sigma}_{\mu}^{-} \hat{\sigma}_{\mu}^{+}, \hat{\rho} \}$ describes the collective dissipator and indices B, D correspond to the bright and dark states in the new basis. The bright state in this basis will have an enhanced decay rate $\Gamma_B = 2\Gamma$, which is twice the linewidth of a single qubit. Conversely, the dark state will become completely decoupled from the waveguide, with no intrinsic decay rate $\Gamma_D = 0$.

This phenomenon can be understood by considering the symmetries of the setup. The two qubits experience the same phase of the photon traveling through the waveguide at the qubit frequency. Therefore, the waveguide can only induce transitions in the symmetric state $|B\rangle = |eg\rangle + |ge\rangle$, which is the symmetric superposition of the ground and excited states of the qubits. Additionally, the decay of the qubits in the symmetric state will constructively interfere, enhancing the emission rate. In contrast, the decay rate of the anti-symmetric state $|D\rangle = |eg\rangle - |ge\rangle$ is opposite to the symmetry of the bright state and will destructively interfere, thereby suppressing the emission rate and coupling to the drive field. In Fig. 3.3 we solve the effective master equation for a system with two qubits separated by distance λ in steady state using the Quantum Toolkit in Python (QuTip) [29]. From the simulation we obtain the lowering operator determining the scattering properties of the drive tone, leading to the simulated resonance features. The two-qubit bright state obtains twice the linewidth of a single-qubit transition, the dark state is not visible as it is decoupled from the waveguide propagating photons.

3.2.2 Coherent Exchange Coupling

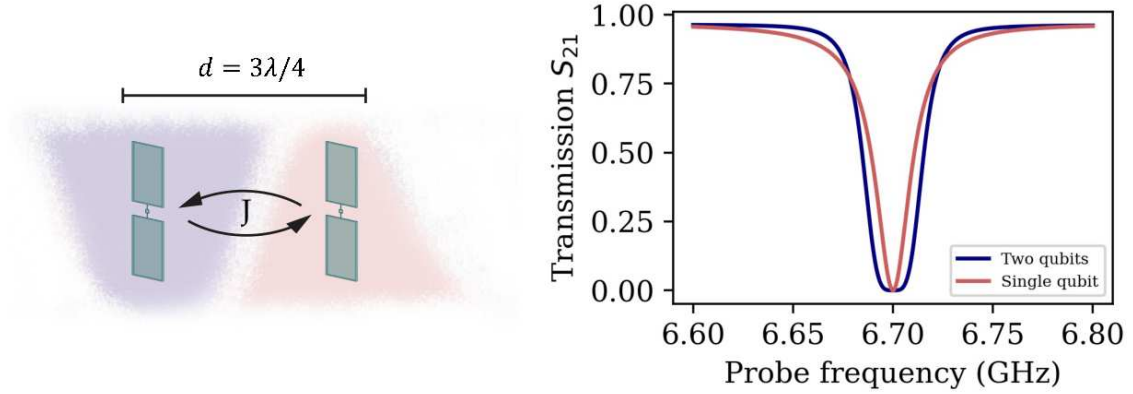


Figure 3.4: Two qubits placed at an effective separation $d = 3\lambda/4$ tuned into resonance do not show signs of super- or subradiant transitions. The exchange of virtual photons results in the hybridization of new eigenstates, which are split by the exchange coupling J . As a consequence, the resonance shape becomes distorted.

Consider a scenario with the same setup as in the previous section. Now, we have two resonant qubits effectively separated by a distance of $d = \frac{3\lambda}{4}$ relative to the qubit frequency. In this case, the correlated dissipation $\gamma_{j,k}$ is absent and the coherent exchange coupling $\tilde{J}_{j,k}$ is maximized. The interaction term from the Hamiltonian eq. 3.32 in the rotating frame takes the form

$$\hat{H}_I/\hbar = \sum_{j \neq k}^N \tilde{J}_{j,k} \hat{\sigma}_j^- \hat{\sigma}_k^+. \quad (3.39)$$

In contrast to the case described in previous section, the individual qubits are still independently emitting virtual photons with $\omega \neq \omega_q$, that are then re-absorbed by each other. This exchange of virtual photons leads to qubit-qubit interaction and the two qubits will hybridize into new eigenstates, which are split in energy by $\Delta E = 2\tilde{J}_{j,k}$ with $|J| = \gamma_r/2$. This interaction resembles the Lamb shift observed when qubits are coupled to the same shared electromagnetic field [37]. The same type of interaction occurs for qubits effectively separated by any distance $d = (2n + 1)\lambda/4$, with n being an integer. The overall sign of $\tilde{J}_{j,k}$ will be then positive for even n and negative for odd n . The absence of correlated dissipation is then expected because each qubit is then at node with respect to each other. The effective interaction strength of each qubit to a particular waveguide mode can be expressed as $\tilde{J}_{j,k} = g_j g_k / \delta$, with $g_{j,k}$ the coupling strengths of each qubit and a frequency detuning δ between the qubit and the waveguide frequency. We simulate the transmission spectrum of two qubits separated by distance $3\lambda/4$ in Fig. 3.4 using the QuTip Python package [29]. The resonant feature of the two qubit case obtains distorted lineshape as result of the coherent exchange coupling hybridizing the eigenstates.

3.3 Direct Capacitive Coupling

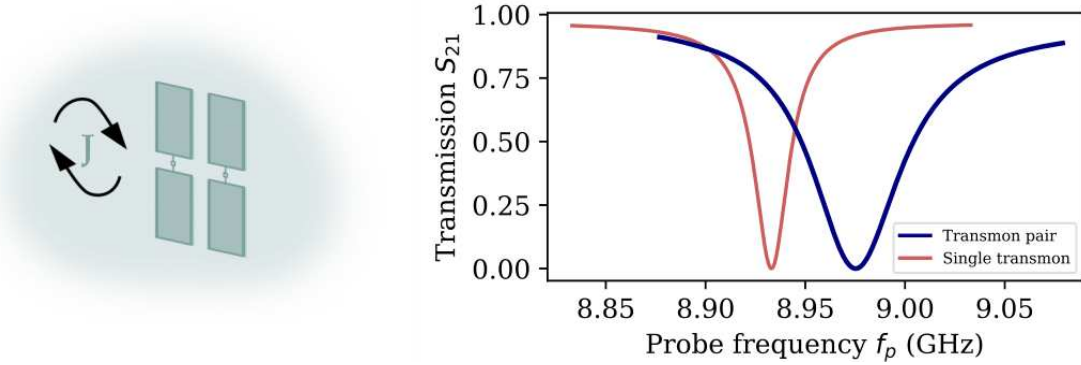


Figure 3.5: Due to coherent exchange, two qubits at resonance form a bright and dark state. Capacitive coupling of the transmon pads leads to splitting of the newly established eigenstates. The bright state has twice the linewidth compared to individual qubit and is detuned by the coherent exchange coupling \tilde{J} from the bare qubit frequency. The dark state is decoupled from the waveguide transmission and not visible in the spectrum.

Consider a case where two qubits are positioned so closely with respect to the wavelength of the microwave photons propagating through the waveguide, that from the perspective of the photons they effectively occupy the same position. As result, the photon travel time between these qubits becomes negligible. Based on the argument from equation 3.31 and 3.30, the correlated dissipation is then maximized, while coherent exchange coupling is absent. This interaction resembles the case of two qubits effectively separated by a distance λ . Furthermore, the close proximity of the metallic transmon pads results in capacitive coupling, manifesting as coherent swapping of excitations between the pads at a rate $J_{j,k}$. The strength of this coupling depends on both the proximity and orientation of the transmon pads [16, 60]. The capacitive coupling between the qubits is similar to waveguide-mediated exchange coupling $\tilde{J}_{j,k}$, observed when two qubits are effectively separated by a distance $d = 3\lambda/4$ and the ground and excited states of both qubits evolve into superposition. The symmetric bright state $|B\rangle = (|ge\rangle + |eg\rangle)/\sqrt{2}$ has in-phase oscillating dipole moments and as consequence becomes double the linewidth (and waveguide coupling) in comparison to a single qubit. The anti-symmetric dark state $|D\rangle = (|ge\rangle - |eg\rangle)/\sqrt{2}$ has out-of-phase oscillating dipole moments, which interfere destructively and give rise to a waveguide-decoupled state.

We simulate two capacitively coupled qubits located at the same position with respect to the waveguide-propagating photons in Fig. 3.5. On resonance the splitting of the eigenstates into bright state with twice the linewidth and decoupled dark state is directly observable. The bright state gets detuned in frequency from the bare qubit resonance frequency due to the exchange coupling $\tilde{J}_{j,k}$.

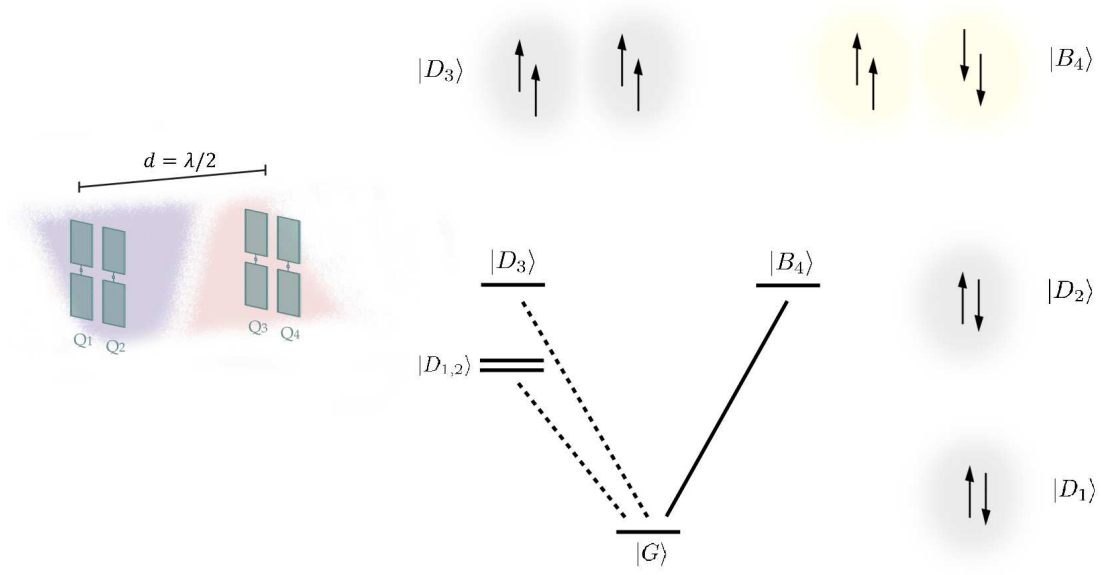


Figure 3.6: Experimental Setup with Four Qubits. In the experimental configuration, two pairs of transmon qubits are positioned within the waveguide at an effective distance of $d = \lambda/2$. This arrangement optimizes the correlated decay while within each pair, a coherent exchange is facilitated due to the capacitive coupling of the qubit pads. The qubits form a collective state comprising of a global delocalized bright state $|B_4\rangle$ with decay rate of 4Γ and decoupled global dark state $|D_4\rangle$, as well as dark state $|D_{1,2}\rangle$ localized at each qubit pair.

3.4 Four Qubits in a Waveguide

In the complete experimental system consisting of two pairs of transmon qubits, we utilize both direct capacitive coupling between the transmon pads within a pair and waveguide-mediated correlated dissipation between the pairs due to the effective pair separation by $\lambda/2$. This separation leads to interference of the local bright states, which decouple the dislocalized global dark state $|D_3\rangle$ and the global bright state $|B_4\rangle$. Each pair still has a local dark state $|D_{1,2}\rangle$, which is decoupled from the waveguide and therefore is not affected by waveguide-mediated interactions.

All states within the state manifold of the full experimental system share a common ground state $|G\rangle$. The dark states constitute a decoherence-free Hilbert subspace because they remain decoupled from the waveguide and the noise, allowing them to relax into $|G\rangle$. Their coherence is only limited by non-radiative decay γ_{nr} and internal qubit dephasing γ_ϕ . These local and global dark states hold promise as a universal quantum computation platform in waveguide QED [46], where the local dark states could serve as a computational basis, while the bright state would be used for readout. By applying a 2π pulse to the global dark state $|D_3\rangle$ from the ground state, we can introduce a phase shift, allowing the implementation of a CPhase gate. We will discuss potential applications and future work in the chapter 6.

Experimental Platform

To perform experiments with superconducting circuits, we need to consider more than just basic building blocks of quantum circuits and waveguide QED. The operations are taken in the microwave regime and while many microwave components are commercially available, the core elements of this experiment - transmon qubits and waveguides, are custom built at the facilities of the university and tailored to specific needs of the experiment. In this chapter, we will provide a brief overview of these elements, including aspects of the setup for qubit control and driving.

In our experimental setup, precise measurements require a low-noise cryogenic environment. To achieve this, we built the waveguide within the mK (millikelvin) stage of a dilution refrigerator, as depicted in Figure 4.1. The copper waveguide and Al/AlO_x/Al Josephson junctions need to be cooled below the critical temperature for superconductivity in order to achieve lossless transmission and ensure minimal energy dissipation of the qubits. However, to achieve superconductivity and reach small levels of quasiparticle excitations, we do not necessarily need to reach mK temperatures; for example, aluminum has a critical temperature of 1.2 K. Generally, it is necessary to cool down the experiment to such low temperatures to avoid thermally exciting the qubits [28]. As described in the section 2.2.1 transmon qubits can be modeled as an anharmonic oscillator. The energy level spacing is the largest between the ground state $|g\rangle$ and the first excited state $|e\rangle$. To prevent exciting this transition, we estimate the necessary cooling temperature based on the condition that the energy level spacing $\sim \hbar\omega$ must exceed the thermal excitation energy of the environment $\sim k_B T$. For typical transmon transition frequencies, this leads to temperatures around 30 – 20 mK below which the quantum system can be initialized in the ground state [55]. The cryostat is thermally insulated by filling it with vacuum and covering it with three layers of protection shields. In addition, the experiment is enclosed in a μ -metal can to shield against external magnetic flux. For qubit control and readout cryogenic wiring is installed, attenuated after each cooling state of the cryostat to minimize the thermal noise photons leaking into experiment, discussed in more detail in section 4.4.

4.1 Rectangular Waveguide

In the field of cavity quantum electrodynamics (QED), researchers trap ions or atoms in optical cavities to shield them from dissipation into the environment. In contrast, in waveguide QED, the quantum emitters are directly coupled to the open environment -

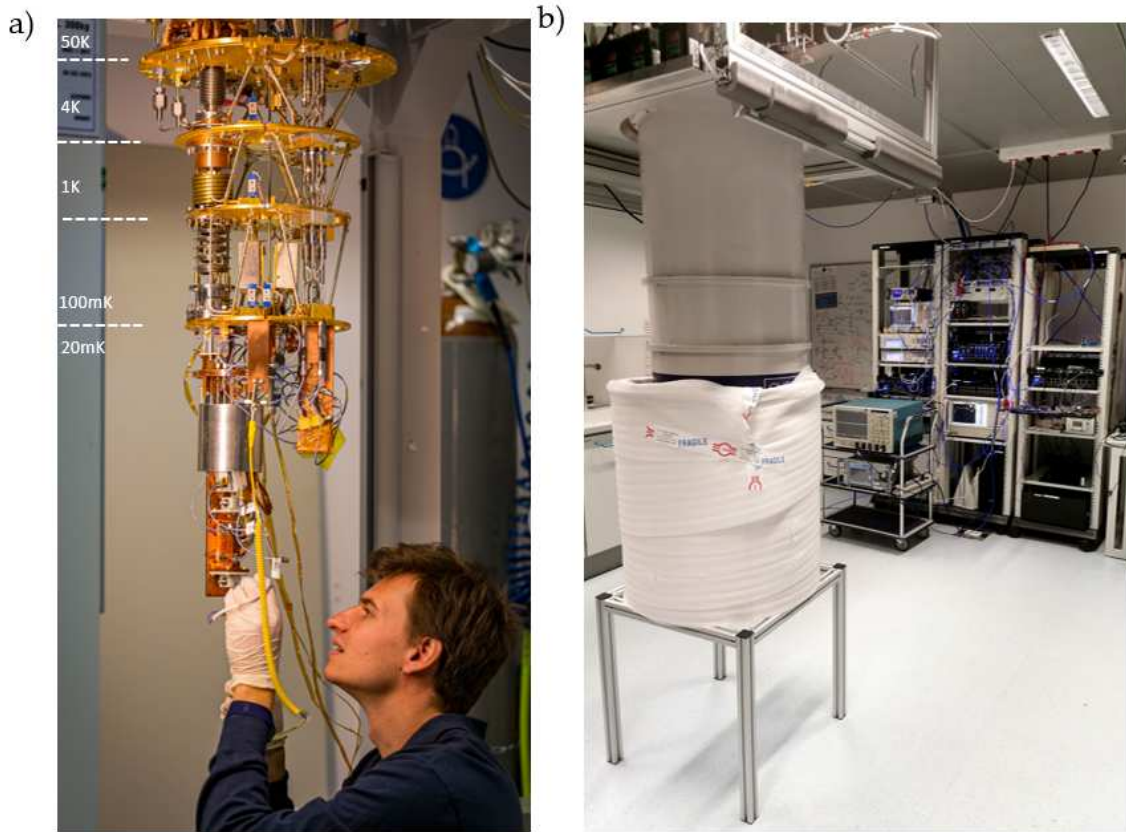


Figure 4.1: Dilution Refrigerator. Experiments must be cooled down to millikelvin (mK) temperatures to avoid thermal excitation of the qubits and protected from magnetic flux noise. **a)** Dilution refrigerator with the shields open and changes being implemented on the experiment, mounted at the lowest cooling stage. Picture taken by David Jordan. **b)** Closed cryostat with an additional μ -metal layer for better flux noise protection and microwave electronics in the background used for readout and control of the experiment.

the waveguide itself. Rectangular waveguides are hollow tubes with open ends and superconducting walls, allowing them to efficiently transmit microwaves with quality factors of several 10^7 and very low attenuation constants [36]. The dimensions of the waveguides are in order of the largest electromagnetic mode that can be transmitted, resulting in waveguide-size dependent cut-off frequency. The most important design parameters of waveguides are thus the width a and the height b of the waveguide, see Fig. 4.2. The finite length c of a waveguide requires the use of adapters for the matching of impedance, since the impedance of the waveguide $Z \sim 500 \Omega$ and the coaxial lines connected to the input and output of the waveguide have an impedance of $Z \sim 50 \Omega$. Imperfections in impedance matching results in building of standing-waves inside the waveguide.

Each waveguide propagating mode has its specific polarisation and can be broadly categorized into either mode with no electric field component (TE) or no magnetic field component (TM) in propagation direction. Waveguide modes with no electromagnetic field component (TEM) can not be excited in our experiment, because they require a sec-

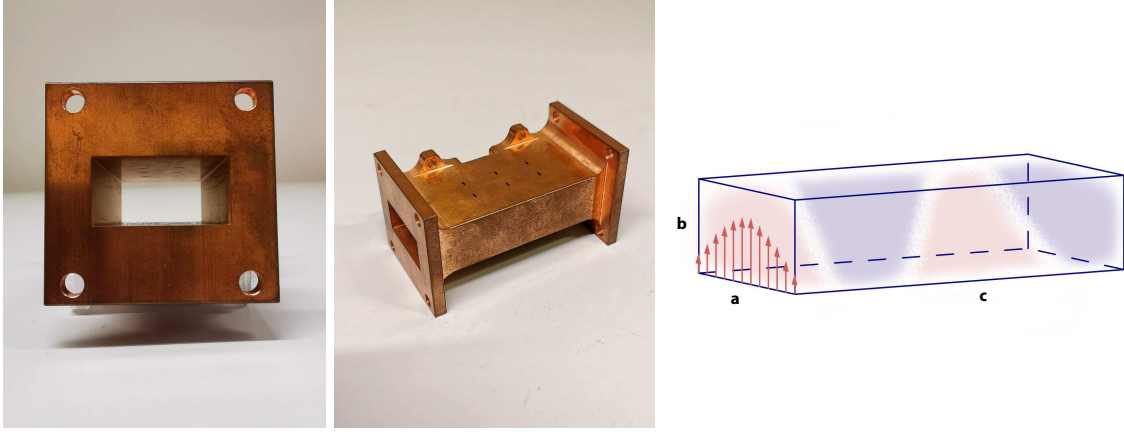


Figure 4.2: WR90 Waveguide. Top and a cross section view of the WR90 waveguide made out of high purity copper. Schematic picture of a rectangular waveguide (right). The different colors of the propagating field mode indicate a change in phase of the field. The field lines represented by the arrows correspond to the fundamental mode.

ond conductor. The TE modes in the waveguide have only a magnetic field component $H_z(x, y, z) = h_z(x, y)e^{-i\beta z}$, where we have introduced the propagation constant

$$\beta = \sqrt{k^2 - k_c^2} = \sqrt{k^2 - \left(\frac{m\pi}{a}\right)^2 - \left(\frac{n\pi}{a}\right)^2}, \quad (4.1)$$

where $m, n \in \mathbb{N}_0$ and the cut-off wave number $k_c = \sqrt{k^2 - \beta^2}$. The TE mode has to fulfill the reduced wave equation [38, 50]

$$\left(\frac{\partial^2}{\partial x^2} + \frac{\partial^2}{\partial y^2} + k_c^2\right) h_z(x, y) = 0. \quad (4.2)$$

Only a wave with wavevector k larger than the cut-off wave vector k_c can propagate through the waveguide. The smallest wave mode that can propagate through the waveguide is referred to as the fundamental mode [38]. For the internal waveguide dimensions $a > b$, the frequency of the fundamental mode can be expressed as

$$f_{c,10} = \frac{1}{2a\sqrt{\mu\epsilon}}, \quad (4.3)$$

where μ represents the permeability and ϵ is the vacuum permittivity. In the case of a rectangular waveguide with $a > b$, the fundamental cut-off frequency depends only on the width a and the electromagnetic constants μ and ϵ . In our experiment we use a WR90 waveguide with inner volume dimensions of 10.2 mm 22.9 mm 100 mm, which leads to lowest cut-off frequency of $f_{c,10} = 6.546$ GHz. Next higher mode cut-off frequency is $f_{c,20} = 13.091$ GHz for the TE₂₀ mode, but due to design parameters of the transmons used in our experiment we operate only in range 6 – 8 GHz. Frequencies above the cut-off propagate through the waveguide according to the propagation constant $\beta = \sqrt{k^2 - k_c^2}$,

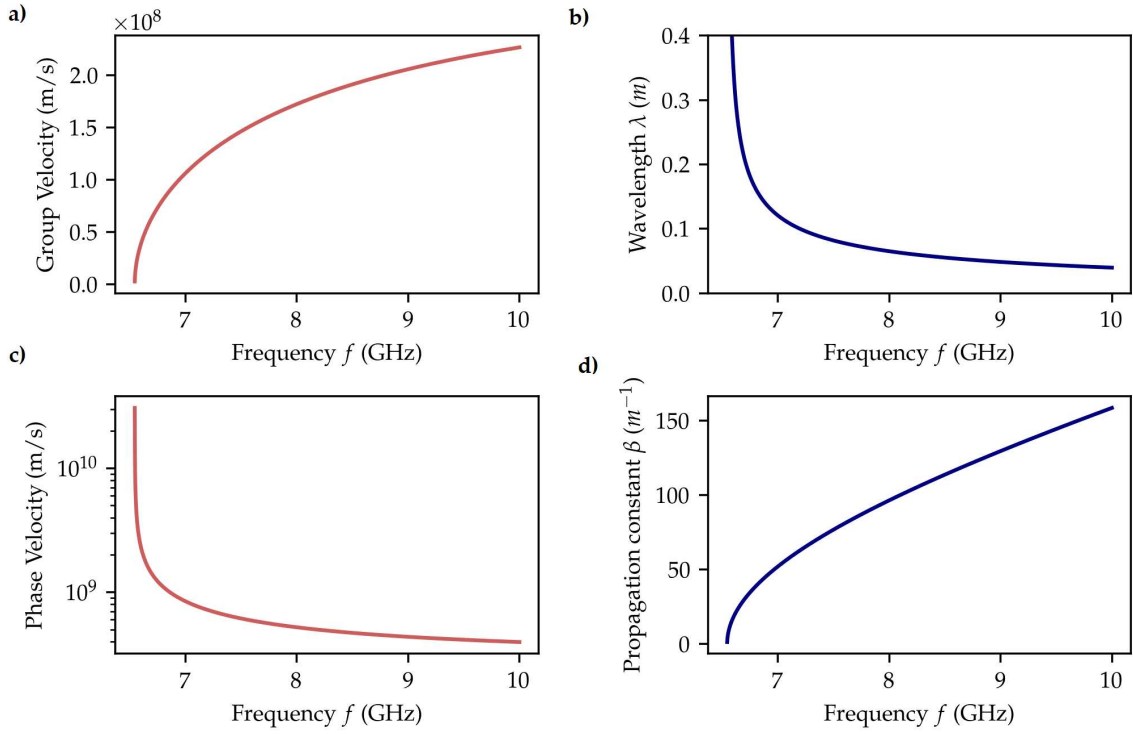


Figure 4.3: Parameters of the WR90 waveguide. **a)** The characteristic group velocity v_g of microwave photons passing through the waveguide is approaching the speed of light $c = 3 \cdot 10^8$ m/s for high frequencies. **b)** The characteristic wavelength in the waveguide as function of frequency approaching 0 at the waveguide cut-off. **c)** The phase velocity of the photons in the waveguide is faster than the speed of light. **d)** The propagation constant β is showing a non-linear dispersion around the fundamental cut-off frequency 6.5 GHz.

with a wave vector given by $k = \omega \sqrt{\mu\epsilon}$. When passing through a waveguide, the wavelength of a plane wave propagating in vacuum $\lambda = 2\pi/k$ needs adjustment to $\lambda = 2\pi/\beta$ due to the constraints introduced by the waveguide. The propagation constant, including the characteristic velocities and wavelengths are shown in Fig. 4.3.

4.1.1 Sideport Driving

In the previous chapter, we explored how two identical transmon qubits on resonance create a manifold of collective states, consisting of a bright state $|B\rangle$ and a dark state $|D\rangle$, due to direct capacitive coupling 3.3 or waveguide-mediated interactions 3.2.1. The dark state is an anti-symmetric superposition and has no waveguide coupling rate, meaning that it cannot be coherently driven via the waveguide propagating photons. For this purpose, we introduce a sideport for each pair of qubits in the setup. The sideport pin is placed off-center on the z -axis of the pair 4.4, such that it creates a local microwave field gradient across the qubit pair and is able to drive the anti-symmetric dark state. The field applied through the sideport will be exponentially attenuated due to the orthogonal orientation with respect to the propagation direction of the waveguide. Because of this fact we are able

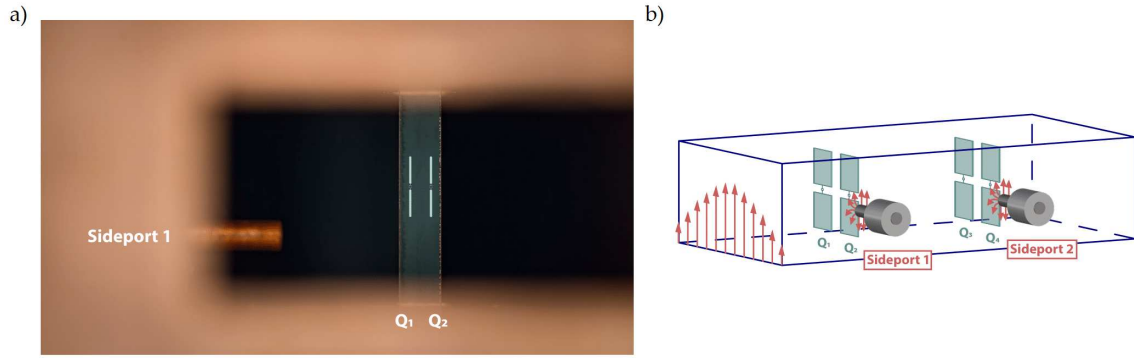


Figure 4.4: The Sideports. Each transmon qubit pair is equipped with a sideport. The sideport creates a gradient field across the qubit pair, which allows for driving of the asymmetrical sub-radiant transition. **a)** A picture of the sapphire chip containing the qubit pair and a nearby sideport. Photo taken by David Jordan. **b)** Illustrated picture of the waveguide with qubit pairs, sideport lines and the propagating field. The field symmetry of the sideport driving field does not coincide with the waveguide propagating mode and is exponentially attenuated. This allows for pairwise dark state driving.

to drive the qubit pairs independently with no observed cross-talk between the sideports. The coupling of the sideport pin to the qubit is given by the distance and orientation of the pin. Each pair has thus slightly different coupling as caused by the imperfections of the experimental setup. We compensate for this by calibrating and sending different absolute powers through the port. Figure 4.4 a) shows picture of a qubit chip and its respective sideport taken through an open side of the waveguide.

4.2 Transmon Qubits

The transmon qubits have been designed specifically for needs of this project and custom built in Quanten-Nano-Zentrum Tirol cleanroom facilities of University Innsbruck. The fabrication of qubits uses modern photolithographic techniques adapted from the complementary metal oxide semiconductor (CMOS) industry. Josephson junctions, the key nonlinear element of superconducting qubits that makes the circuit anharmonic, have been fabricated of aluminum with an aluminium-oxide barrier and covered in a sapphire wafer. The fabrication was conducted by members of our research group and thus the precise fabrication steps will not be covered in this chapter. For detailed explanation of the fabrication procedure we refer to [60].

4.2.1 Qubit Design Parameters

One significant advantage of superconducting qubits is their flexibility in designing a wide range of Hamiltonian parameters. By combining various circuit elements and coupling techniques, we can tailor an 'artificial atom' to meet the specific requirements of a given

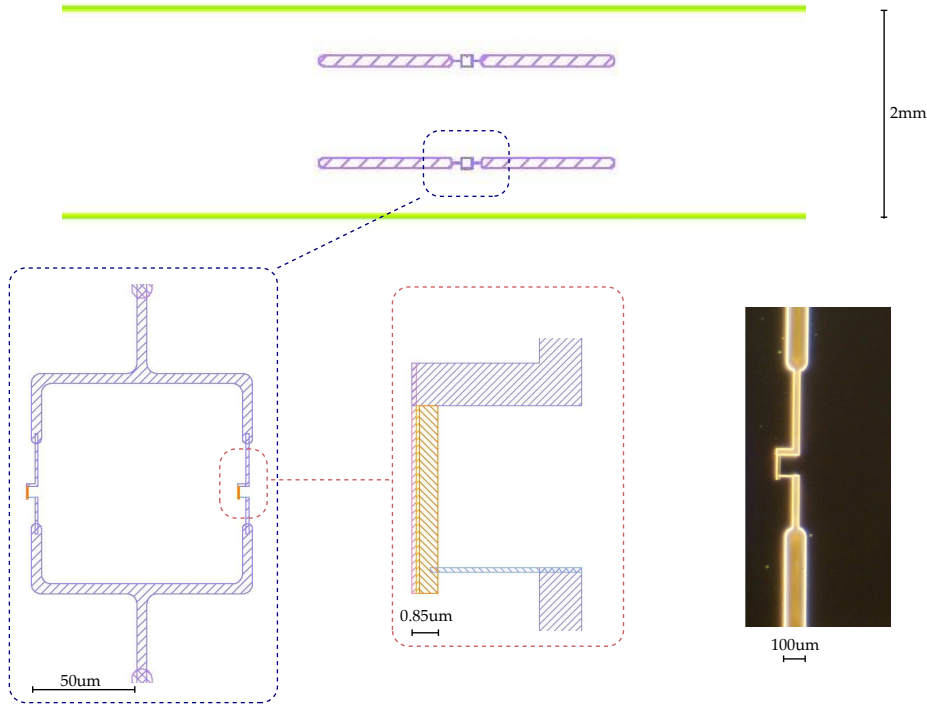


Figure 4.5: Design of the Qubit Chip. Design of two transmon qubits on a single sapphire chip, the green lines are chip edges that will be cut out of the sapphire wafer. A zoom in to one of the qubits reveals the individual Josephson junctions sitting in parallel forming a SQUID loop. Optical micrograph picture of the junction after vaporization (right).

project. The qubits are designed to have a favorable transmon ratio $E_j/E_c > 40$ and desired coupling strengths. The resonance frequency of the qubit must also be supported by the microwave setup. We simulate the qubit using Ansys HFSS ¹ to obtain these values for a system without any decoherence effects. We draw the metallic transmon pads, simulated as a perfect conductor, the sapphire chip and the vacuum ² filling the waveguide, and simulate the transmission parameter S_{21} of the qubit, as shown in Fig. 4.6. The data obtained from the simulation are then fitted using a circle fit routine to determine the resonance frequency. Assuming a junction inductance $L_j \approx 7$ nH, we calculate the Josephson energy $E_j = 23.35$ GHz and the charging energy $E_c = 341$ MHz, resulting in a transmon ratio of $E_j/E_c = 68$. A single transmon qubit in this design would have a linewidth of 54 MHz without any decoherence effects. A standard design of the transmons used in this experiment is shown in Fig. 4.5.

Another critical factor in junction design is qubit aging. Even when the sample is predominantly kept in a vacuum environment, the oxide layer between the aluminum pads

¹<https://www.ansys.com/products/electronics/ansys-hfss>

²All materials used from HFSS database.

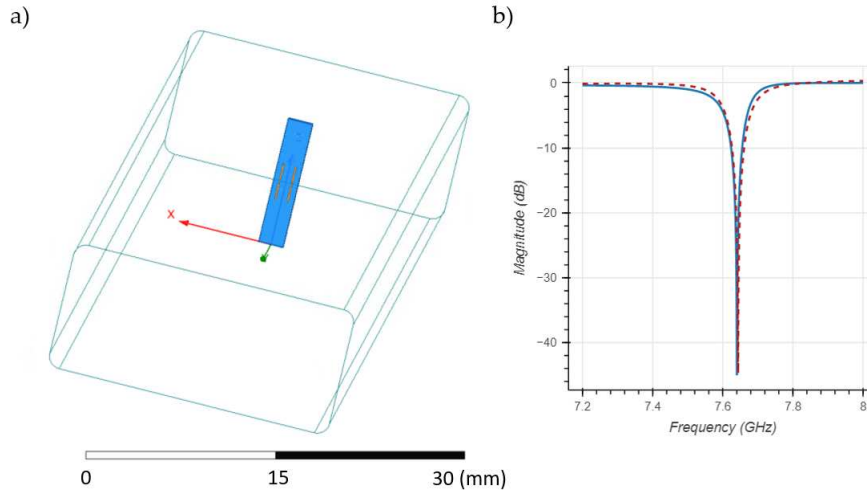


Figure 4.6: Qubit Simulations. a) Simulation of a transmon qubit pair embedded in a sapphire chip. b) Simulated resonance feature of the qubit, fitted with a circle fit.

gradually thickens over time, resulting in an increased resistance [49]. This effect saturates at approximately a 10% rise in resistance as the sample is cycled in the cryostat.

4.3 Coil Setup

A significant limitation of our setup is the qubit cross-talk. The qubits are positioned so closely to each other that independently addressing them during flux tuning becomes challenging. This issue is particularly pronounced within each qubit pair, although cross-talk also occurs between the pairs. To address this issue, we have designed a coil setup based on magnetic flux simulations. This arrangement includes two coils for each qubit pair, symmetrically spaced relative to the qubit positions, allowing us to optimize individual qubit control. When a current flows through each coil, it generates a characteristic dipole magnetic field. The orientation of the qubit SQUID loops is such that they face the waveguide transmission. Consequently, a qubit positioned directly beneath a coil experiences magnetic field lines pointing downward but not through the SQUID loop. In contrast, the neighboring SQUID loop in the pair is slightly off-center, resulting in magnetic field lines that have a component passing through the SQUID loop. In this way we have aimed to implement differential qubit flux tuning.

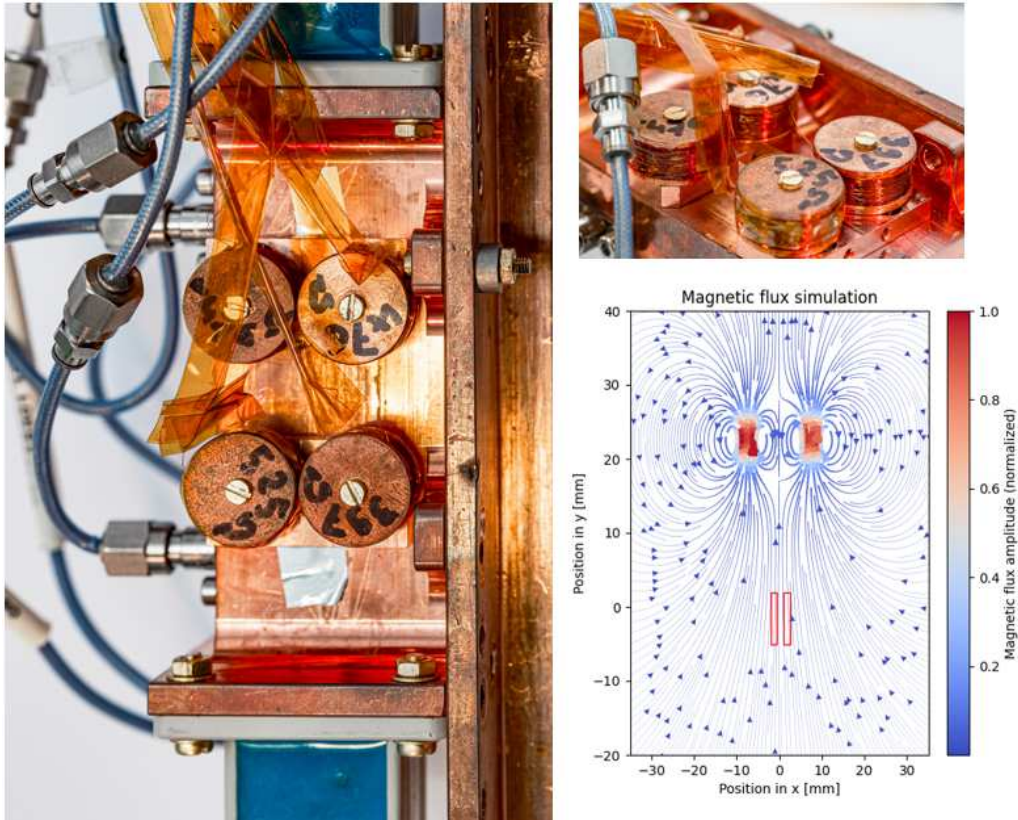


Figure 4.7: Coil setup. Setup of four coils mounted on top of the rectangular waveguide designed to tune the four qubits (left). Side view of the coil setup (top right). Pictures taken by David Jordan. Magnetic flux simulation with Magpylib (bottom right). For visualization two rectangular red loops resembling the qubits were added to the plot. The field lines are solutions of Biot-Savard law.

Furthermore, we utilize two distinct flux tuning regimes to control and optimize the collective bright and dark states within each qubit pair. When both coils are ramped up with the same polarity and identical current steps, their resulting magnetic flux fields overlap, significantly affecting both qubits in the pair. We refer to this tuning regime as "common mode" tuning and use it to adjust the effective emission frequency of the pair. On the other hand, we can selectively ramp one coil in the pair against the other, creating a "differential mode" tuning scenario. In this configuration, the magnetic fluxes from the coils interact and only the flux difference at the qubit position influences the pair. We utilize this regime to precisely adjust any detunings in individual qubit frequencies, bringing both qubits within the pair into perfect resonance. While common tuning regime creates strong magnetic flux, which is also influencing the distant qubit pair, the differential tuning regime is only impacting the local pair due to its small differential field strength. Figure 4.7 shows the coil arrangement on the top of the waveguide and a magnetic flux simulation for a qubit pair in a common tuning regime. To optimize flux tuning, we conducted magnetic flux simulations based on Biot-Savart law using the MagpyLib Python package³. Due to

³MagpyLib Python package 2023, <https://magpylib.readthedocs.io/en/stable/>

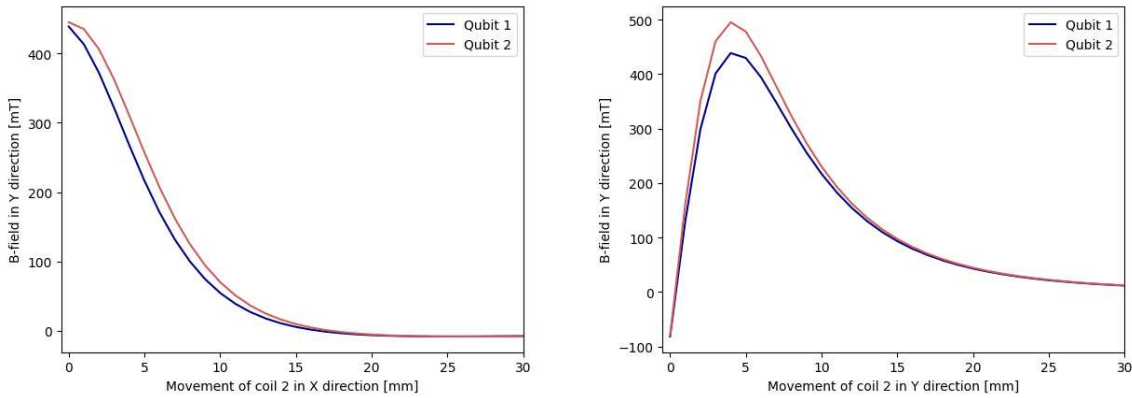


Figure 4.8: Magnetic Field Simulation. Simulating magnetic field at the position of each of the qubits, while sweeping through the position of a single coil to achieve the largest flux difference between the qubits. The Y-axis is perpendicular to the waveguide propagation direction, pointing across the qubit pair. The X-axis is parallel to the waveguide transmission direction with qubit SQUID loop facing the transmitting waves. The B-field is decreasing as the coil moves further away from the position of the qubits.

physical size constraints in our setup, we systematically explored the positions of individual coils. For each position, we calculated the magnetic flux component flowing through the SQUID loop of each qubit. Figure 4.8 illustrates the strength of magnetic flux when a coil is moved perpendicular to the waveguide transmission direction (left) and along the waveguide direction (right). It can be seen that for specific arrangement the coil creates a flux difference at the qubit positions. We use the coil position creating the largest flux difference and optimize in the same manner also the coil sizes. Once the best configuration was established, we designed the coil bodies using Solidworks, depicted in Fig. 4.9 b) and had the university workshop construct them from copper. Subsequently, we wound a thin $50\mu\text{m}$ superconducting wire around each coil body, applying varnish and a layer of cigarette paper after each winding to ensure protection and prevent shorting. The coil winding process is depicted in Figure 4.9 a). We wound as many windings as possible to create a strong magnetic flux while avoiding excessive current, which could lead to sample heating.

4.4 Cryogenic Wiring

The rectangular waveguide, serving both as a readout and sample holder, is fixed to the bottom “base” plate of the Triton DU7 – 200 Cryofree dilution refrigerator, operating at approximately 20 mK. The waveguide is in direct contact with the sample holder, which ensures thermalization of the sample. The sapphire chips containing qubits are attached to copper clamps that hold them in the center of the waveguide and thermalize to the waveguide with the help of small screws that tighten them on the side. The qubit control and readout is achieved by sending radio frequency (RF) signals and direct current (DC) sources applying flux bias to frequency-tunable qubits. The control electronics are

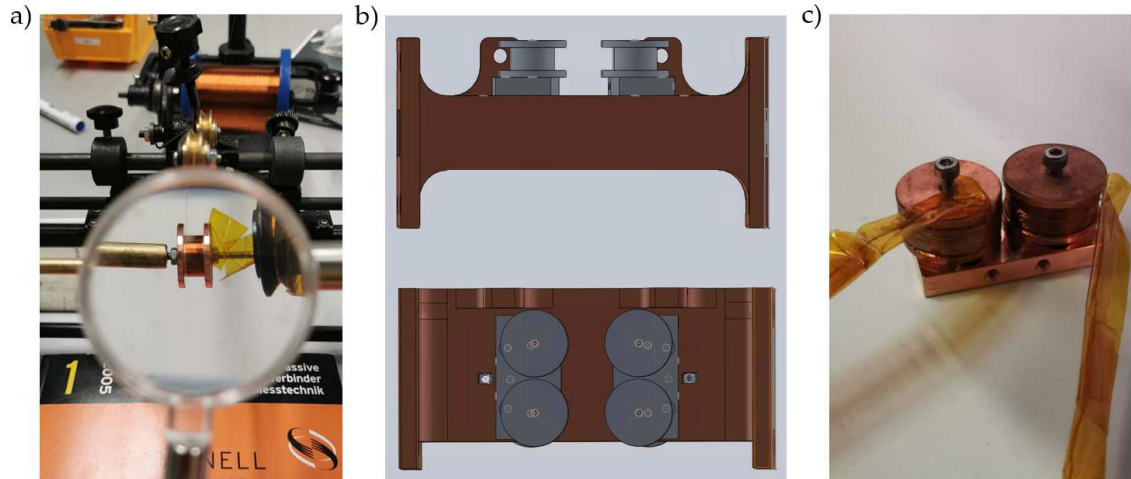


Figure 4.9: Coil Fabrication. a) Winding of a coil with a thin superconducting $50\mu\text{m}$ wire. On average 72 m of wire has been wound on each coil. b) Solidworks drawing of the waveguide with the designed coil arrangement. The qubits are positioned in the center of the waveguide. c) Mounting of coils on fabricated copper bodies getting prepared to be mounted on top of the waveguide.

located at room temperature, so in addition to keeping the experiment thermalized, we need to ensure that we protect it from the noise coming through the control drive lines and output lines [21, 55]. For this purpose we use self-built microwave wiring including filters, attenuators and isolators. The input lines are connected to refrigerator stages with higher temperature and will therefore introduce a thermal noise to the experiment. We attenuate the signal after each stage to reduce leakage of thermal photons through the lines. The main source of thermal noise through the output line is the high electron mobility transistor (HEMT) amplifier. We do not want to attenuate the output signal, so for the output lines we use cryogenic isolators, that allow transmission out of the experiment but strongly attenuate in opposite direction.

Additionally to the protection from thermal noise, we use 4 – 8GHz bandpass filters Microtronics BPC50403-G084 on each driving line to attenuate the microwave noise. The last microwave element, besides attenuation before the lines enter the can with experiment is a home-built Eccosorb filter, which absorbs the high-frequency infrared noise, which would lead to additional losses due to excitation of quasiparticles across the superconducting band gap [21, 45].

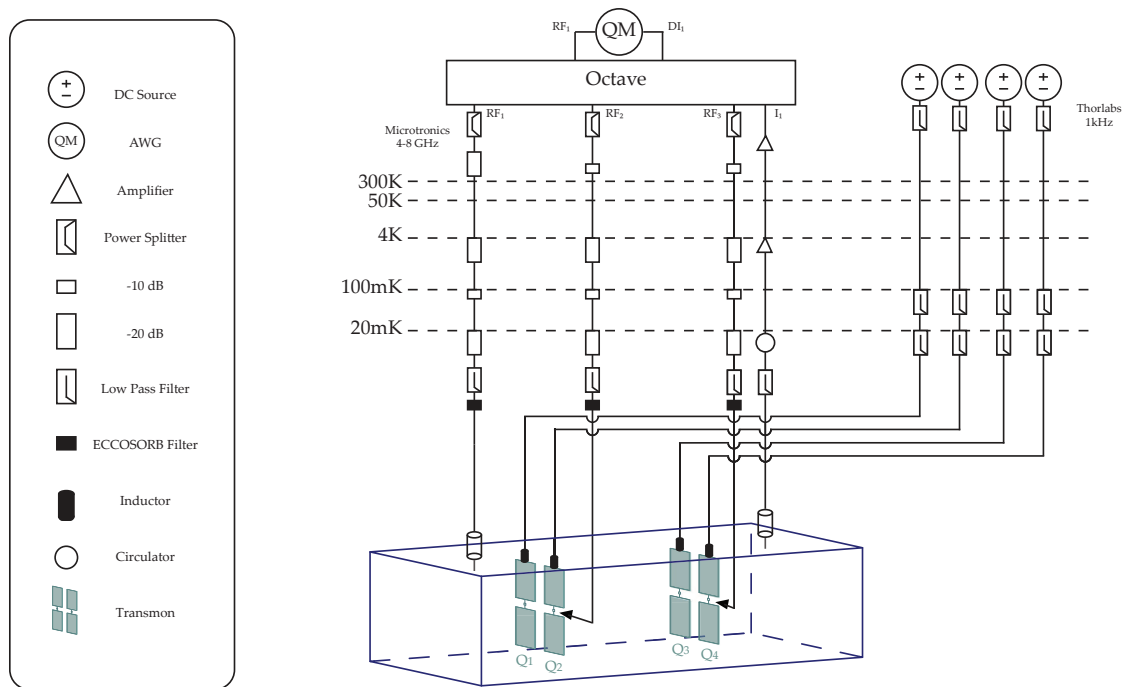


Figure 4.10: Schematic of the wiring. The schematic includes the Octave, which is an integrated IQ-mixing circuit, the microwave electronics at room temperature, drive and output lines with cryogenic attenuation, filters and amplifiers.

We tune the qubits in frequency by applying current from Keysight B2902A SMU and Yokogawa GS200 DC sources through the coils mounted on top of the waveguide. Each DC line is equipped with a room temperature Thorlabs EF110 lowpass filter. The experiment is controlled either using continuous wave (CW) measurements with a vector network analyzer (VNA) or using pulsed sequences from an arbitrary waveform generator (AWG). As AWG we use Quantum Machines OPX+ platform, which includes an analog to digital converter (ADC) and is extended by Quantum Machines Octave - an integrated IQ-mixing circuit for up- and downconversion of the signal. Figure 4.10 shows a simplified schematic overview of the cryogenic wiring for time domain measurements with AWG.

Characterisation of Multi-Qubit System in Rectangular Waveguide

In this chapter, we outline the measurement methods [41] used to characterize the experimental system. We begin by characterizing a pair of transmon qubits using continuous-wave (CW) or long-pulse measurements. Subsequently, we investigate interactions between dark and bright states. Leveraging these interactions, we extract the population of the decoherence-free dark state and perform coherent control using pulsed sequences and time-domain measurements. Finally, we extend our analysis to the full experimental system, which consists of four transmon qubits and present our findings.

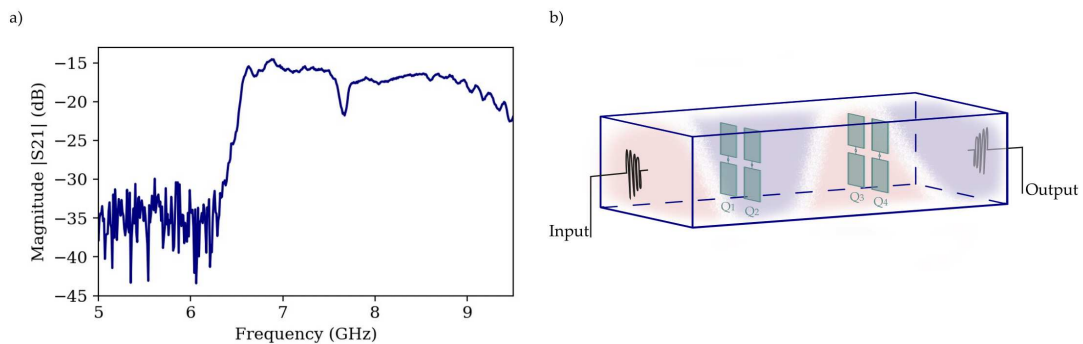


Figure 5.1: Waveguide Transmission. a) The S_{21} measurement of the waveguide transmission. Waveguide has a cut-off frequency at approximately 6.5 GHz below which the transmission exponentially decays to the level of background noise. A bright state transition of a qubit pair is visible at around 7.8 GHz as a dip in the transmission spectrum. b) A schematic drawing of a waveguide transmission measurement.

5.1 Waveguide QED with Two Transmon Qubits

Two identical qubits on resonance interact due to close vicinity of the metallic transmon pads, leading to coherent exchange swapping of photons. The qubits get new collective eigenstates comprising of a symmetric bright state and anti-symmetric dark state. In following we characterize this state one-excitation manifold, beginning with flux tunability and following with dependence on drive power and spectroscopy measurements. The qubits

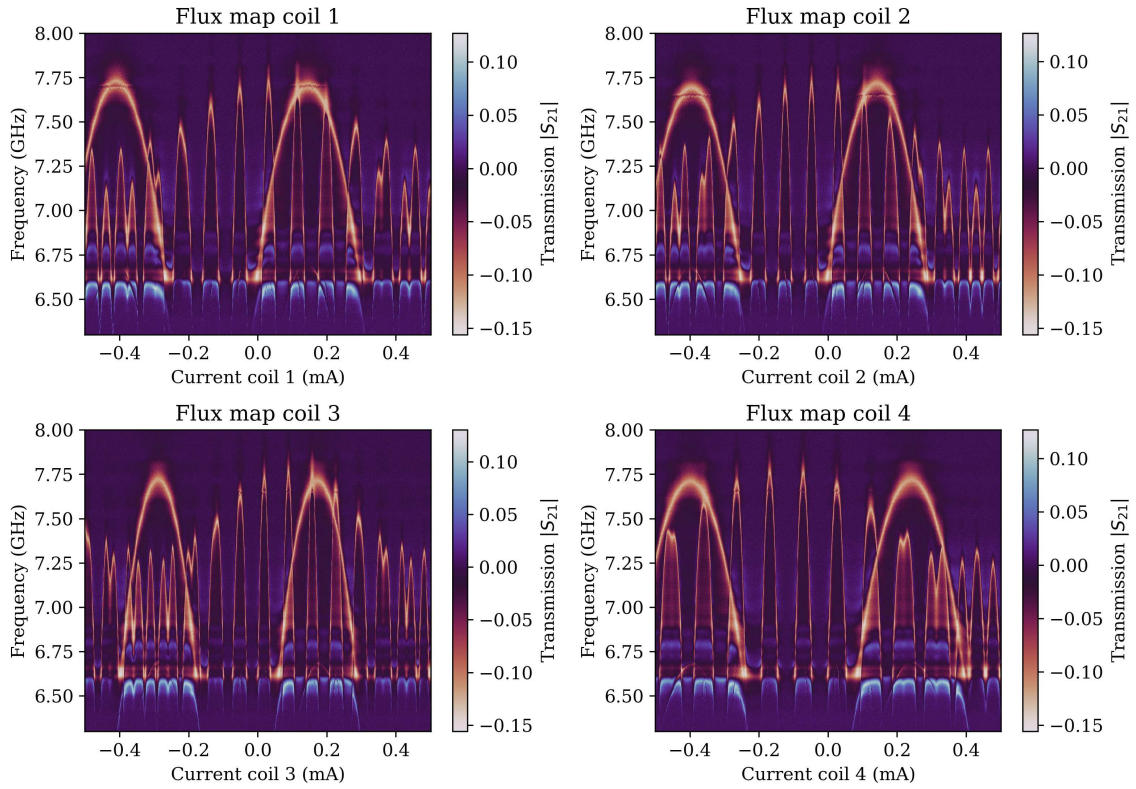


Figure 5.2: Flux maps. Single coil is tuned across range of 1mA and all other coils are turned off. **a)** Coil 1 is positioned directly above qubit pair 1. Due to the close proximity of the qubits on the chip and the strong coupling $\tilde{J}_{j,k}$, both qubits within the pair exhibit similar tuning behavior. This manifests as the fast oscillating resonances. On the opposite side of the waveguide, another qubit pair is affected by crosstalk, resulting in slower oscillating resonances. **b)** Due to their symmetrical arrangement and close proximity, the flux map of Coil 2 closely resembles that of Coil 1. However Coil 2, positioned on one side of the pair, tunes the nearer qubit slightly more than the other. The difference can be seen when comparing the plot for coil 1 and coil 2 in the region around 0.4 mA, where the individual qubits detune from one another. **c)** Arrangement analogue to a) but for the qubit pair 2. This coil has slightly more turns than the others, resulting in a stronger field and shorter oscillating periods. **d)** Analogue to b) on the pair 2.

have been specifically designed to have a strong coupling rate $\tilde{J}_{j,k}$ in order to achieve better driving. This, however, leads to qubit resonances becoming hybridized, making it challenging to distinguish individual qubit resonances.

5.1.1 Flux Tuning

Qubits with Josephson junctions built in SQUID configuration can be made frequency tunable by applying external magnetic flux, as can be seen from eq. 2.21. For availability

reasons, we used two different yet comparable DC current sources, Keysight B2902A and Yokogawa GS200 to drive current through the superconducting coils built on top of the waveguide housing for flux-tuning. Adding an experimental parameter requires calibration; thus we measure a flux map for each coil, while keeping the other coils inactive. In Fig. 5.2, we change the current flowing through a single coil from -0.5 mA to 0.5 mA, while measuring the waveguide transmission parameter $|S_{21}|$. Through these measurements, we gain insight into the response of the qubit system in the presence of external magnetic flux. Specifically, we determine the current settings for tuning qubit to a specific desired flux spot, explore the tunability range of the qubits and analyze their oscillation periods.

The qubit pair positioned directly beneath the coil being swept experiences a strong magnetic flux. This effect manifests as fast-oscillating resonances on the flux maps, depicted in figure 5.2. Conversely, the pair located on the opposite side of the waveguide encounters a much weaker field due to its greater distance from the coil and is visible as the slow oscillating large resonances. As we increase the absolute value of the current applied through the coil, the magnetic flux increases and consequently, the flux difference at the qubit positions becomes larger. We observe the qubits within a local pair tuning apart as the absolute current increases.

Common and Differential Coil Tuning

Besides applying flux bias with a single coil, we also utilize two distinct flux tuning regimes to control and optimize the collective multi-qubit states. Two coils in symmetric arrangement are mounted on top of the waveguide housing for each qubit pair. In common tuning mode we apply current through both coils in the same polarity. We calibrate for imperfections and differences in the number of windings of each coil by counting the periods in single coil flux map 5.2 and calculating the step in current accordingly. The magnetic fields in common tuning mode overlap and tune both qubits in a pair with the shared common field. Figure 5.3 a) shows a flux map measured in common tuning mode. The fast-oscillating narrow resonances are the local pair located directly beneath the coil, experiencing a strong field and responding to even small differences in the applied magnetic flux. Due to cross-talk is the distant qubit pair from the opposite side of the waveguide also visible. It shows up as the slower oscillating periods, because its experiencing a weaker field as a consequence of its distance to the coils.

In common tuning mode, we can tune the collective bright state to a desired frequency. Using the differential tuning mode, we manipulate the qubits by ramping the two coils in opposite polarity. With differential tuning, we fine-tune the local qubit pair using only the flux difference between the fields produced by the coils (see Figure 5.3 b). The differential flux is small in amplitude, ensuring it does not influence the distant pair on the other side of the waveguide, which appears as a vertical line in the measurement. After tuning the pair in common mode to the desired frequency, we can mitigate small detunings in individual qubit frequencies using differential mode. To assess the detuning in frequencies, we measure the relaxation time T_1 of the dark state, aiming to maximize it for a “perfectly dark” dark state.

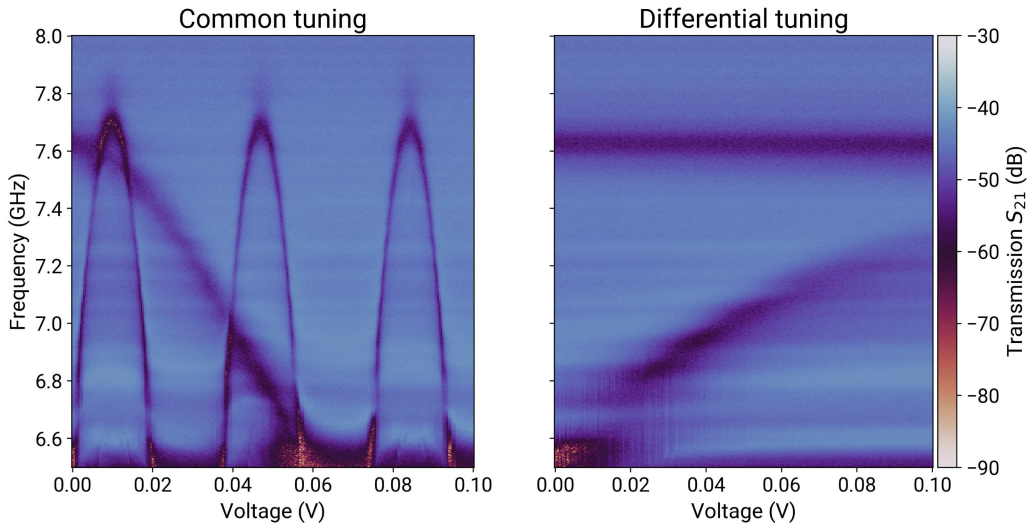


Figure 5.3: Common and Differential Flux Tuning. **a)** Flux map utilizing common coil tuning regime. Both coils on a pair are synchronously tuned with the same current and same polarity. The local pair is visible as fast oscillating narrow resonances, while the distant pair, affected by cross-talk, oscillates more slowly due to a weaker magnetic field (the large slow tuning resonance). **b)** Flux map measured utilizing the rejection tuning regime. Two coils within a pair are tuned using the same current but with asynchronous polarity. As a result, the pair is exclusively tuned based on the flux difference. Specifically, only the local pair undergoes tuning in this regime, as the flux difference is insufficient to affect the pair on the other side of the waveguide. The plot consists of two consecutive measurements taken at different frequency ranges due to device limitations. The variations in contrast are likely attributed to differences in calibration.

5.1.2 Power Saturation

When a microwave photon travels through the waveguide at resonance frequency of the qubit, it becomes absorbed by the qubit and subsequently re-emitted in both forward and backward directions, with a phase difference. In the forward direction, the re-emitted photon interferes destructively with the propagating signal due to the phase difference. As a result, we observe a reduction in the amplitude of the transmitted microwave signal, manifesting as a Lorentzian dip in the transmission spectrum centered around resonance frequency of the qubit. Conversely, in the backward direction, between the waveguide input and the qubit position, the re-emitted photon interferes constructively. Performing effectively as a perfect mirror for low drive powers at the qubit resonance frequency [4, 39]. The depth of the observed dip in the transmission spectrum depends on two key factors: the amplitude of the signal propagating through the waveguide and the specific characteristics of the qubit. The reduction in transmitted signal is decreased if the excited qubit dephases before re-emitting the photon or if it radiates the excitation to a parasitic two-level system. Additionally, when the incoming signal amplitude is so large that the qubit cannot re-emit the photon before another one arrives, we observe power-dependent saturation of the resonant dip, as illustrated in Figure 5.4. Along the power saturation effect it can

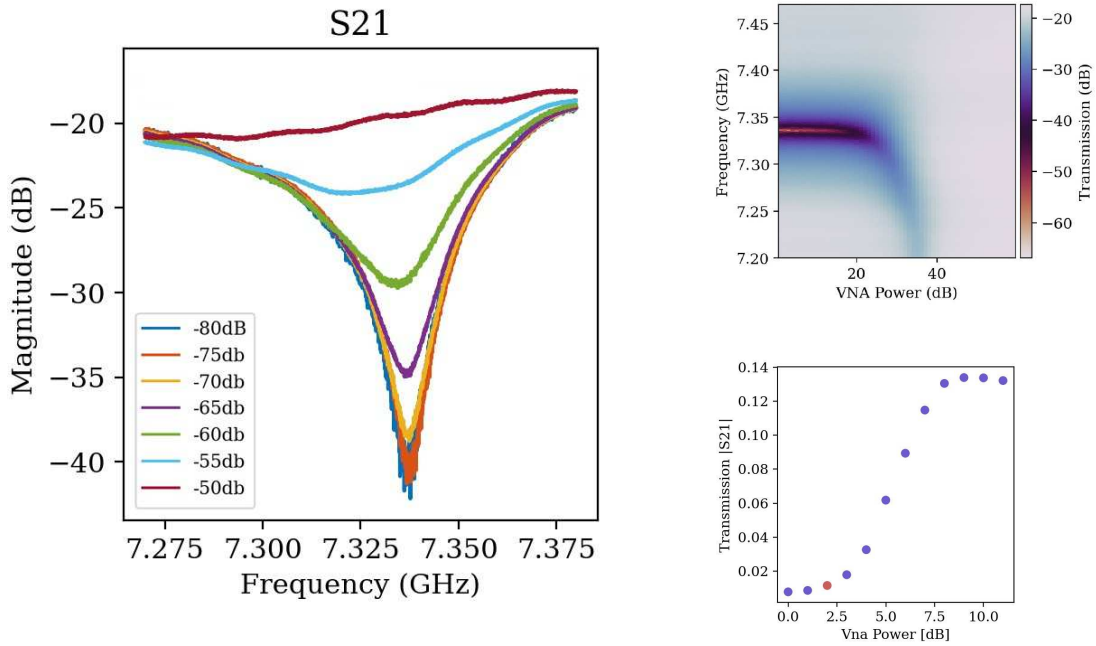


Figure 5.4: Power Saturation. The probe power is increased as the probe frequency is varied across the resonance frequency of the qubit pair. For a statistical single photon probing power, the qubit pair absorbs and re-emits one photon at a time. As the probe power rises, a greater number of photons travel through the waveguide. This leads to saturation of the qubit resonance, where some photons remain unabsorbed due to the saturated $0 - 1$ transition and reach the end of the waveguide increasing the $|S_{21}|$ coefficient. At high probe power, the qubit resonance completely disappears from the transmission spectrum. (bottom right) Minima of the resonance features are extracted for increasing probe powers, a single photon power that would be selected for the measurement is indicated by red color.

be observed that the resonance feature is also power-broadened and shifted in frequency, similar to AC-Stark shift, with increasing transmission amplitude.

5.1.3 Circle Fits

From the observations of qubit resonance features in waveguide transmission measurements, we can extract the fundamental coupling strengths of the qubit. The waveguide transmission parameter S_{21} is a complex number with information about both the amplitude and phase of the signal scattered on the qubit transition. In a notch configuration, the spectral shape of a resonator coupled to transmission line closely resembles that of a qubit transition at low drive power $\gamma_r \gg \Omega$. Thus we extract the qubit quality factors Q with the help of the circle-fit notch routine [32, 51]. For the intended experiment, the frequency corresponding to the qubit separation of $\lambda/2$ is in particular interest. Figure 5.5 shows the circle fits of a waveguide transmission measurement at this frequency, in which we fit the equation 3.36 to the measurement data. From 5.5 we were able to extract

the quality factors for a two-qubit bright state: $Q_l = 60$, $Q_c = 62$ and $Q_i = 2428$ and a linewidth of approximately 120 MHz at frequency of 7.36 GHz. This value is close to expectations based on the design parameters of the qubit, where the linewidth of a single qubit transition was simulated to be 54 MHz without decoherence. The resonance feature is still likely hybridized, due to the strong coupling rate $\tilde{J}_{j,k}$.

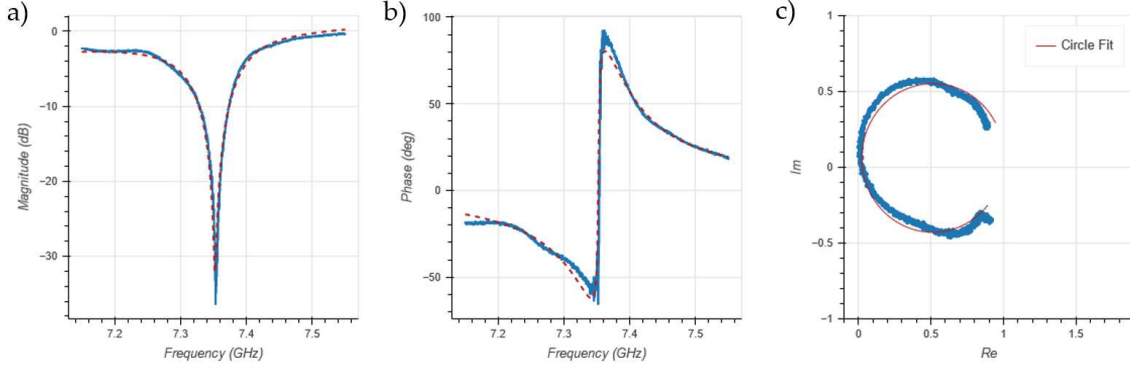


Figure 5.5: Circle Fit Routine Measurement of a single transmon pair plotted in blue, red dashed line represents the fit. **a)** The transmission coefficient $|S_{21}|$ at the resonance frequency of the qubit pair is more than 30dB smaller than the probe power. The bright state resonance has a linewidth of 120 MHz. **b)** The propagating signal experiences a phase shift of 180° after interacting with the qubit pair. **c)** When applying a circle-fit routine to the complex scattering parameters, we address the asymmetric lineshapes arising from interference with standing waves in the microwave background.

5.1.4 Avoided Crossing

In this chapter, we have analyzed the control and characteristic properties of a two-qubit bright state. Now, our focus shifts to utilizing the interaction between bright and dark states to study and perform coherent operations on the waveguide-decoupled dark state. To determine the interaction strength between these two states, we continuously tune two transmons forming a pair in and out of resonance, while measuring the transmission through the waveguide. If there was no coupling, that is, no interaction between the bright and dark state, the two states would simply cross, intersecting at the point of zero-frequency detuning. However, because of the direct capacitive coupling arising from the proximity of metallic transmon pads, the qubit resonances do not cross. Instead, they approach closely and diverge, maintaining a minimal separation. This phenomenon is known as avoided crossing or anti-crossing [8, 52]. On resonance, excitations can coherently swap between the two transmons, leading to hybridization of the transitions and formation of new eigenstates. In the detuned case the branches represent individual qubit $|0\rangle - |1\rangle$ transitions. The frequency detuning at the point of minimal separation corresponds to $2\tilde{J}_{j,k}$, where \tilde{J} represents the coupling rate between the states. We measure the avoided crossing for both pairs of qubits, as depicted in Figure 5.6 and determine the coupling strength between the bright state $|B\rangle$ and the dark state $|D\rangle$ to be $\tilde{J}/2\pi \approx 500$ MHz.

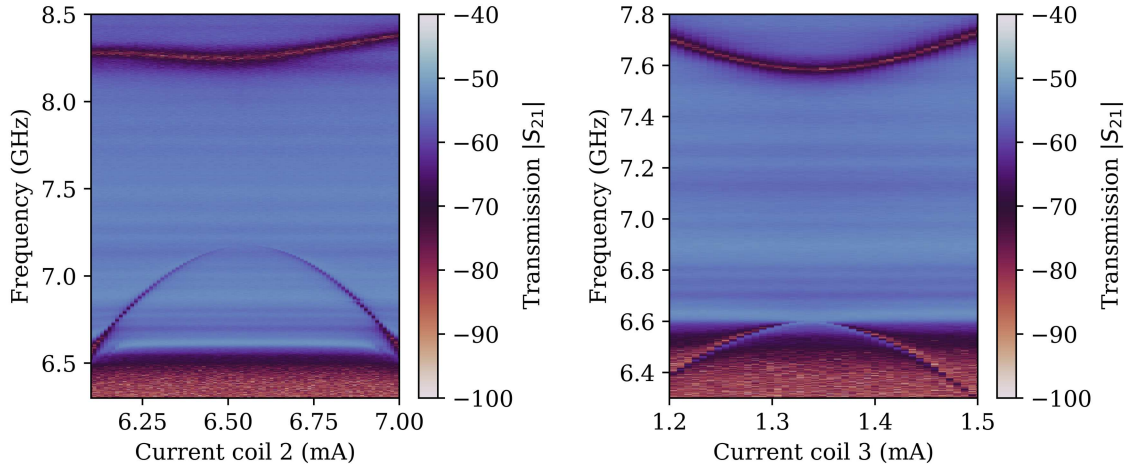


Figure 5.6: Avoided Crossing of Two Qubits. We tune the two qubits in a pair in and out of resonance and observe the avoided crossing of the bright and dark state, revealing the coupling strength $\tilde{J}/2\pi \approx 500$ MHz for both transmon pairs.

We take advantage of this interaction to read out the population of the waveguide-decoupled dark states via performing waveguide transmission measurements monitoring the level of the corresponding bright state.

5.1.5 Dark State Spectroscopy

After determining the bright state frequency and the transmission amplitude used for readout, we proceed with dark state spectroscopy measurements to identify the resonance frequency of the dark state and calibrate the power of the signal sent through the sideport. In this measurement, we send a range of frequencies through the sideport, subsequently measuring the waveguide transmission parameter S_{21} at the bright state frequency after each sideport pulse. We specifically probe the dark state approximately 1 GHz below the bright state frequency, leveraging our knowledge of the coupling between the two states (as described in section 5.1.4). Figure 5.7 illustrates the dark state spectroscopy measurement, along with the corresponding pulse sequence. The blue line represents dark state spectroscopy at low sideport drive power. At the resonance frequency of the dark state transition the readout level experiences a jump to approximately double the readout level, indicating that the dark state has been excited. As we move to higher frequencies, the readout amplitude returns to the previous level due to frequency detuning. At high drive powers (red line), the dark state resonance experiences power broadening and a level from a higher-excitation manifold appears in the spectroscopy, as the dark state transition becomes saturated.

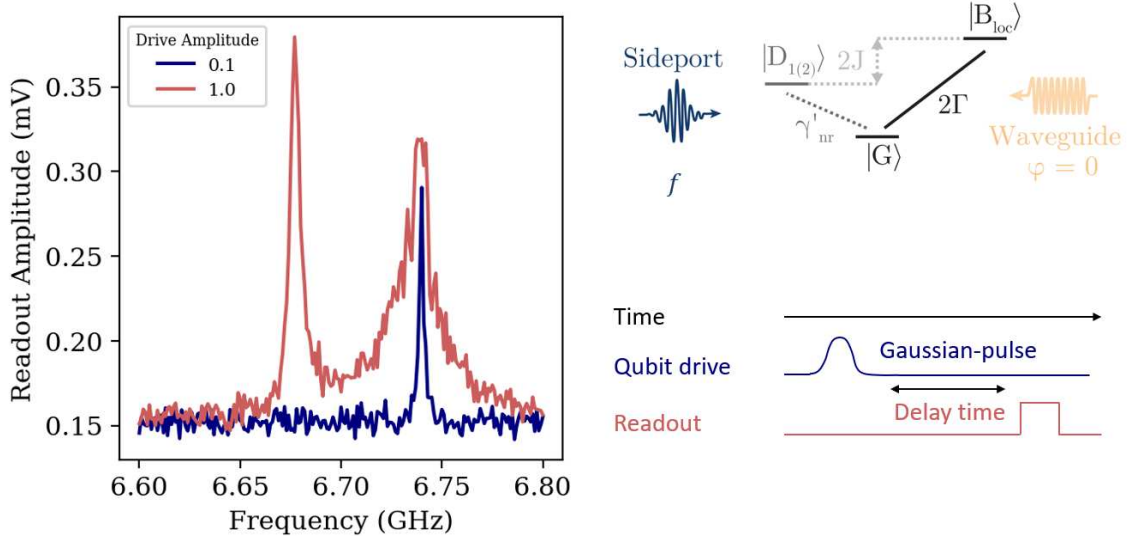


Figure 5.7: Dark state spectroscopy. A range of frequencies are transmitted through the sideport. Corresponding to each frequency, a readout pulse is sent through the waveguide at bright state frequency. Level of the bright state is increased when the signal transmitted through sideport matches the resonance frequency of the dark state (left). At higher drive amplitude the resonance peak undergoes power broadening and multi-photon peaks appear. (right) Diagram of the level scheme with a pulse sequence used in the measurement, captured by an oscilloscope. A Gaussian pulse is sent to excite the darkstate, followed by a square readout pulse through the waveguide.

Anharmonicity of the Local Dark State

In this experiment we did not characterize the entire state manifold including the multi-photon states, but considering insights from the previous version of the experiment [60], there might be several higher-excitation states. While these higher excitation states do not play a central role in the current experiment, it is important to consider them when determining pulse lengths and drive amplitudes. We have observed states of higher-excitation manifold in the measurements when performing transmission measurements in the high-power regime, as depicted in Fig. 5.8 b). To further investigate states that are close in frequency to the dark state, we conducted a two-tone spectroscopy in which we measured the waveguide transmission parameter with VNA at low-power levels. while applying a microwave signal through the sideport using an external signal generator EXG at the dark state frequency.

As the amplitude of the EXG signal increases we can observe saturation of the transition $|G\rangle - |D_{1,2}\rangle$ and appearance of a hybridized higher-excitation state with anharmonicity of approximately 120 MHz to the dark state, shown in figure 5.8 a). The shape of the resonant feature of the higher-level state is distorted because at this flux bias point it was located below the waveguide cutoff frequency.

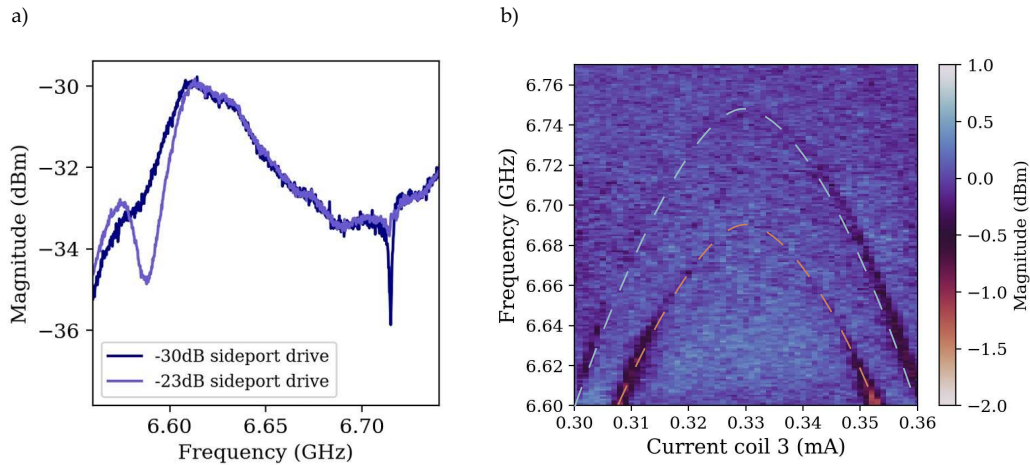


Figure 5.8: Dark State Anharmonicity. **a)** Two tone spectroscopy. Waveguide transmission is measured using VNA at low probe power, while simultaneously the dark state is pumped with an external signal generator through the sideport. When higher power is sent through the sideport, the dark state becomes saturated and a higher-excitation state appears. **b)** A flux map of the dark state at high transmission power without external signal generator. At high transmission power, the dark state becomes likewise saturated, resulting in the emergence of a higher-excitation state. This needs to be accounted for when performing the measurements. A red dashed line indicating the position dark state and blue dashed line the position of the anharmonic state.

5.1.6 Time Domain Characterization

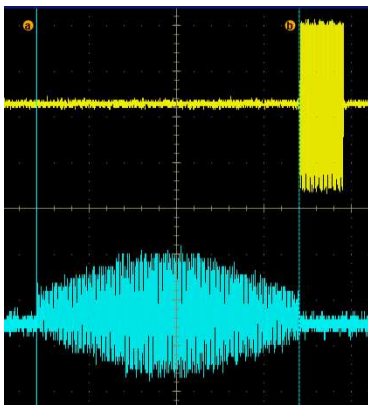


Figure 5.9: Example of a Pulse Sequence Taken by a Signal Analyzer.

Figure 5.9 shows an example of a pulse sequence used to perform measurements in time-domain, 600 ns Gaussian-pulse used to excite the dark state transition (blue) and 100 ns square pulse used for readout measurement through the waveguide (yellow).

Spectroscopic measurements in the frequency domain, taken with small steps across a wide frequency range are typically measured using a continuous wave or long pulses. They serve to characterize the Hamiltonian parameters in a steady state of the qubit. However, when aiming to investigate the dynamics of the system and performing coherent operations on the nanosecond scale, it becomes necessary to use short pulses for the control sequence. For this purpose, we switch from using a vector network analyzer (VNA) to an arbitrary waveform generator (AWG) and IQ mixing scheme (or Octave) to provide read-out and sideport driving.

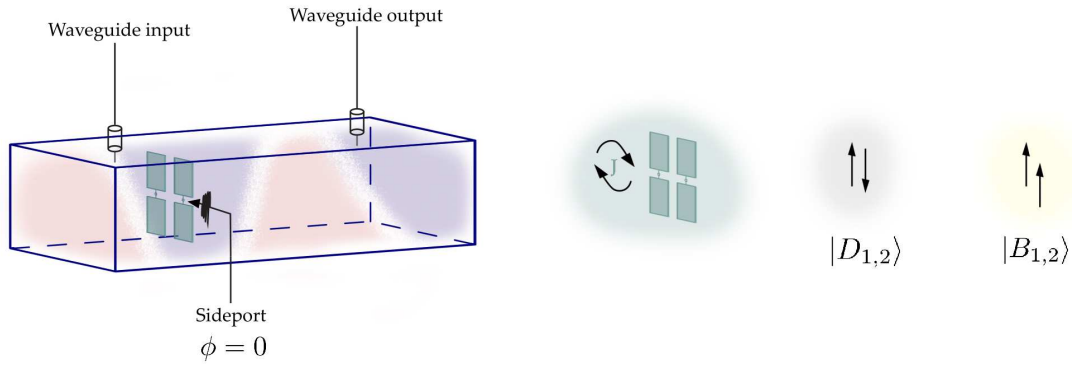


Figure 5.10: Schematic of the Experimental Setup with a Single Transmon Pair. The transmon plates serve as the coupling capacitance leading to coherent exchange coupling. Within the waveguide, only states that align with the phase of the waveguide drive field are excited—this symmetry holds for the capacitively coupled pair. In contrast, the sideport, due to its gradient across the pair, can also excite the antisymmetric states.

Rabi Oscillations

The first experiment in time-resolved setup that we perform to tune up qubit pulses is the power Rabi experiment. In this variant of the Rabi experiment we keep the length of the drive pulse constant, ensuring that it has the same frequency width, but increase the drive amplitude Ω . First, a qubit drive pulse is played through the sideport of a local pair, followed by a waveguide transmission measurement for the readout. The drive pulse is calibrated on the dark state spectroscopy measurements such that a pulse brings the qubit to the excited state; in this case we bring the qubit state from the ground state $|G\rangle$ to the dark state $|D_{1,2}\rangle$ and access the bright state via the waveguide for readout of the dark state population. Between measurements a long wait time is required, typically several T_1 , to re-initialize the system back to the ground state. Figure 5.11 shows a power Rabi measurement in a range of dark state drive frequencies. The figure includes a measurement scheme and a linecut taken at the center frequency. When the drive pulse is detuned from the resonance frequency of the dark state, it is unable to excite the dark state transition. However, at high drive amplitudes it remains to be able to drive the transition, resulting in the characteristic pattern.

Characteristic Qubit Decoherence Times

The characteristic qubit relaxation time T_1 is measured by sending a π -pulse to the dark state via the sideport, exciting the dark state transition and varying the delay time before the readout through the bright state. The best measurement of a single pair T_1 is shown in figure 5.12. Choosing the amplitude with highest dark state population in Fig. 5.11, increases the measurement contrast. The measurement is fitted with an exponential decay

$$y_1(t) = Ae^{-t/T_1} \quad (5.1)$$

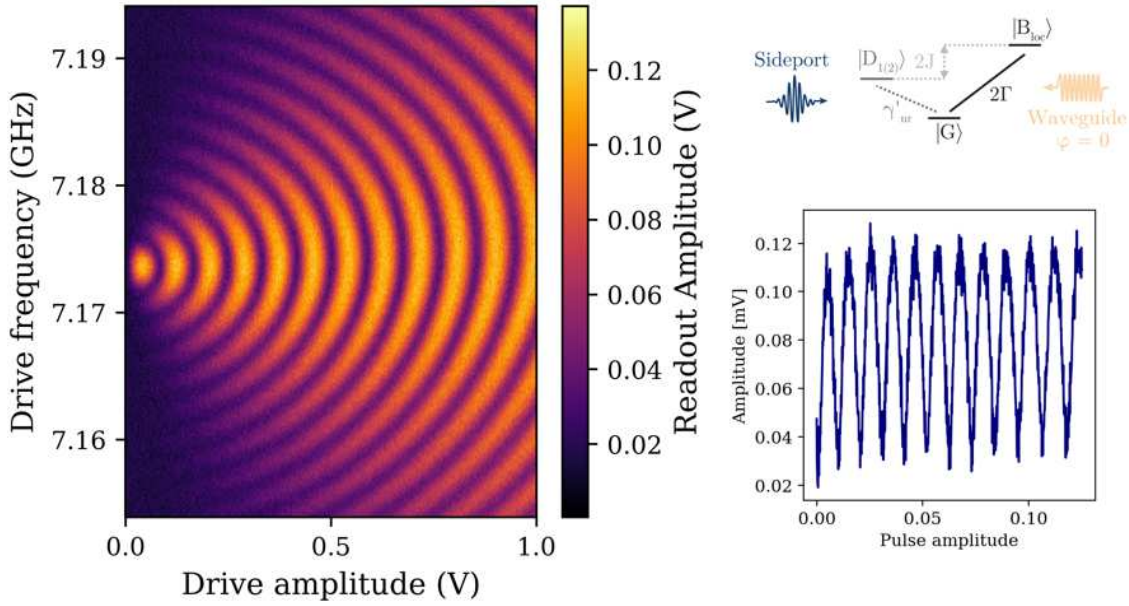


Figure 5.11: Power Rabi Measurement of a Single Qubit Pair. The anti-symmetric component of the sideport drive can be used to drive Rabi oscillations, while simultaneously measuring the waveguide transmission through the waveguide ports. With this measurement scheme we observe Rabi oscillations between the ground state and the local dark state as the pulse amplitude increases. When the frequency of the sideport drive is detuned from the dark state resonance frequency, Rabi oscillations cannot be excited. However, at higher drive amplitudes, they become observable. (right) A linecut through the dark state resonance frequency at 7.173 GHz and a level scheme including the pulses.

to extract the time constant $T_1 \approx 26\mu\text{s}$. Compared to the bright state with linewidth of ~ 120 MHz and a lifetime in the order of nanoseconds, encoding the qubit into the decoherence-free dark state leads to significant improvement in the relaxation time. We characterize the dephasing time of the qubit with the Ramsey experiment. This requires the same setup as for the relaxation time measurement, but a different pulse sequence, as shown in figure 5.13. First the qubit is excited by applying a $\pi/2$ - pulse through the sideport to a superposition state $1/\sqrt{2}(|G\rangle + i|D_{1,2}\rangle)$, that is an equal probabilistic mixture of states, such that one can no longer confidently predict the state. Then after a varying time delay t another $\pi/2$ -pulse is sent to bring the qubit back to the ground state and subsequently immediately performing a readout through the waveguide. We fit the data by exponentially decaying sine function [41]

$$y_2(t) = A + B \sin(2\pi\Delta_d t + \phi) \exp(t/T_2^*), \quad (5.2)$$

with detuning Δ_d and phase offset ϕ to determine the dephasing time $T_2^* \approx 590$ ns. We introduce an additional phase shift to the second $\pi/2$ - pulse to see more oscillations in the measurement and achieve a better fit. We explain the comparably low value of the T_2^* lifetime due to limitations associated with magnetic flux-noise in the dilution refrigerator.

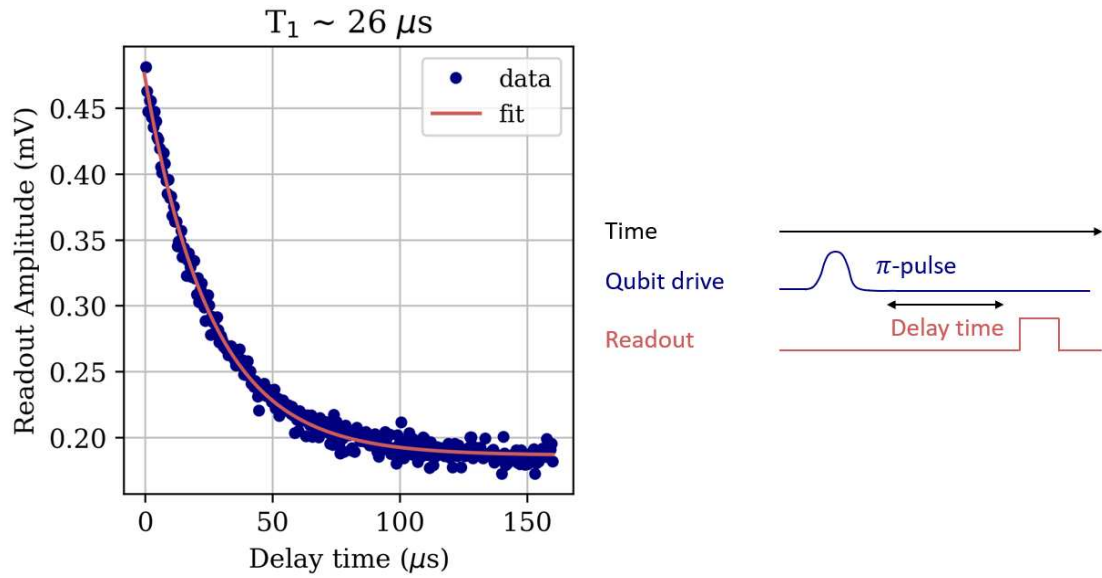


Figure 5.12: The Qubit Relaxation Time T_1 . We apply a π -pulse, determined from the Rabi oscillations, to excite the qubit to the excited state. After a varied wait time, the readout is performed determining the bright state amplitude.

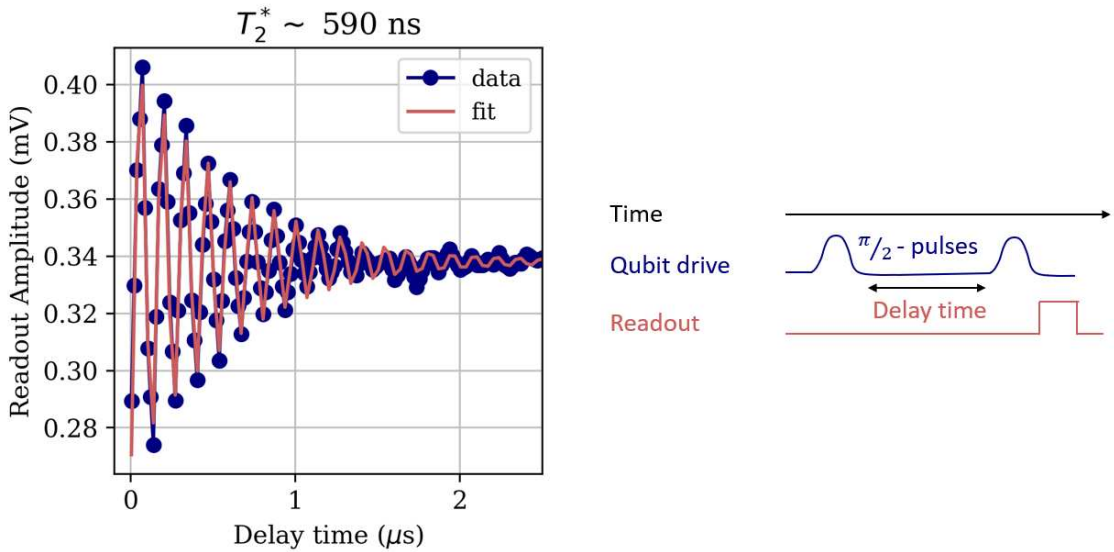


Figure 5.13: The Dephasing Time T_2^* of the Local Dark State. The dephasing time T_2^* can be determined by fitting the data acquired by the Ramsey measurement scheme to exponentially decaying sine function eq. 5.2. A $\pi/2$ -pulse is sent through the sideport exciting the dark state to the superposition, followed by a varied wait time and subsequent $\pi/2$ -pulse to bring the qubit back to the initial state. After each cycle a readout pulse is sent through the waveguide. The parameter T_2^* has a fit error of $2.43 \cdot 10^{-8}$. Schematic of the pulse sequence is shown on the right.

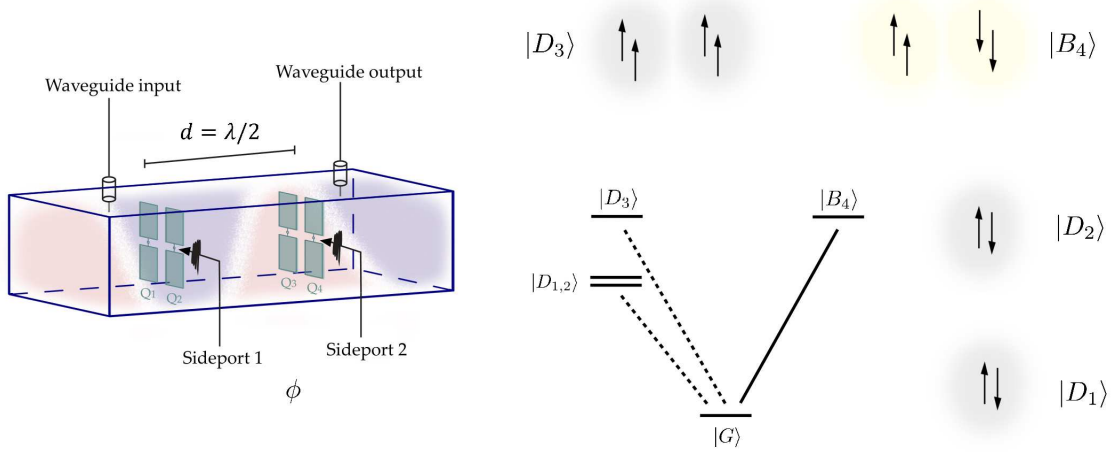


Figure 5.14: The Complete Experimental System with Four Transmon Qubits. Sketch of the waveguide with two transmon pairs including a sideport line to drive the local dark state respectively. A drawing of the level scheme consisting of a local dark state $|D_{1,2}\rangle$ for each pair and a global delocalized dark state $|D_3\rangle$ and global bright state $|B_4\rangle$.

5.2 Waveguide QED with Four Transmon Qubits

To incorporate an experiment that leverages both direct qubit exchange coupling and waveguide-mediated interactions, we employ two pairs of transmon qubits, as schematically shown in Fig. 5.14. These pairs are effectively separated by a distance of $\lambda/2$ to maximize correlated dissipation between them, meaning the local bright states $|B_{1,2}\rangle$ destructively interfere decoupling the dislocalized global four-qubit dark state $|D_3\rangle$ and global bright state $|B_4\rangle$ with a linewidth four times that of a single qubit transition (as depicted in Fig. ??). The state manifold still includes the two qubit local dark states $|D_{1,2}\rangle$ localized at the position of each pair. The only transition visible in the waveguide transmission measurement is between ground state $|G\rangle$ and $|B_4\rangle$. Achieving this requires tuning all qubits to resonance, which presents challenges due to qubit cross-talk. First, we tune the qubits within a single pair to resonance. Subsequently, we utilize common and differential tuning techniques to bring both pairs into resonance at the desired frequency corresponding to a separation of $d = \lambda/2$. To determine this frequency, we need to consider the phase $\phi = 2\pi d/\lambda$, with the pair separation $d = (46 \pm 2)$ mm, that a photon acquires when traveling from one transmon pair to the other [37, 60]. The phase is dependent on the photon wavelength in the waveguide $\lambda = 2\pi v/\omega$, where v describes the phase velocity and ω the angular frequency. For a phase difference $\phi = \pi$ this corresponds to an effective emission frequency $\frac{\omega}{2\pi} = (7.31 \pm 0.06)$ GHz.

5.2.1 Rabi Oscillations on the Collective Dark State

The sideport that creates a gradient field across a pair of qubits is capable of driving the dark state, which is inaccessible through the waveguide due to symmetry restrictions.

Sending microwave pulses at the frequency of approximately 7.32 GHz, corresponding to the effective pair separation of $\lambda/2$, through the sideport excites the transition between $|G\rangle$ and the delocalized four-qubit dark state $|D_3\rangle$, shown in Fig. 5.15. The global bright state $|B_4\rangle$ is degenerate in energy with $|D_3\rangle$, so we cannot use a frequency-selective drive to choose the transition, but we can select the transition by introducing a phase difference between the sideports [60]. Due to the π -shifted symmetry of the respective oscillating dipoles between $|D_3\rangle$ and $|B_4\rangle$, we can coherently scatter photons between the ground state and $|B_4\rangle$ to read out the population of $|D_3\rangle$ via a waveguide transmission measurement. Figure 5.15 shows a power Rabi measurement between the ground state and $|D_3\rangle$ utilizing this readout method. We used a constant-length Gaussian excitation pulse and maintained a phase difference of $\phi = 0$ between the sideports, as the observed oscillations arise from driving with only one of the sideports. A single sideport can excite the global dark state, but leads to a decreased contrast as the bright state $|B_4\rangle$ is also affected by the drive pulse. The amplitude of the signal scattered on $|B_4\rangle$ after dark state excitation does not fully return to the ground state level, potentially due to leakage from $|D_3\rangle$ into $|B_4\rangle$. Nevertheless, we successfully demonstrate coherent control of the collective four-qubit dark state and further investigate the characteristic lifetimes associated with this transition.

5.2.2 Characteristic Decoherence Times of the Collective Dark State

We experimentally determine the relaxation time T_1 of the global dark state $|D_3\rangle$ by sending a Gaussian π -pulse through the sideport to excite the transition from $|G\rangle$ to $|D_3\rangle$. We then vary the delay time before performing a readout via waveguide transmission, measuring the level of global bright state $|B_4\rangle$. The measurement results are shown in Figure 5.16, where we fit an exponential decay (given by Equation 5.1) to the data to extract the time constant, which yields $T_1 \approx 0.7\mu\text{s}$. The relaxation time of the global dark state is significantly shorter than the T_1 time associated with the local dark state in a single transmon pair. However, it is important to compare the relaxation time with that of the global bright state, which has double the linewidth of the bright state in a single pair. Additionally, potential factors such as imperfect matching of the decoherence-free frequency corresponding to the $\lambda/2$ pair separation or detuning of local transmon pairs in frequency, despite our best efforts, may contribute to decrease in T_1 . Furthermore, the measurement of a short dephasing time (see Figure 5.17) also hints at the impact of flux noise as a potential limitation.

To analyze the susceptibility of the global dark state to environmental noise, we perform a dephasing time T_2^* measurement using a Ramsey experiment, following the methodology described in section 5.1.6. We initiate the experiment by sending a $\pi/2$ -pulse through the sideport, preparing the system in an equal probabilistic superposition state $1/\sqrt{2}(|G\rangle + i|D_3\rangle)$. After varying the wait time of the system being in the superposition, another $\pi/2$ -pulse is applied to bring the system back to the $|G\rangle$ state. Subsequently, we perform a waveguide transmission measurement of the global bright state $|B_4\rangle$ to read out the dark state population. The measurement results, shown in Figure 5.17, are fitted using a decaying sine function given by Equation 5.2. From the fit, we determine the parameter $T_2^* \approx 390\text{ ns}$. To achieve a better fit, we applied an artificial phase rotation to the second $\pi/2$ -pulse. Due to background flux fluctuations causing shifts in the resonance frequency,

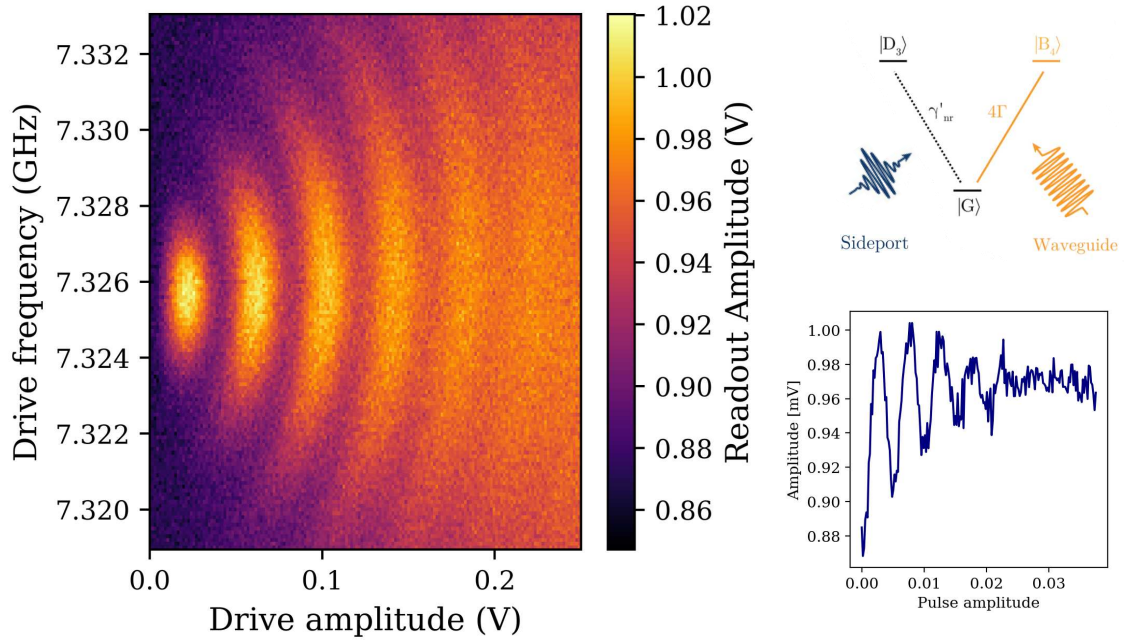


Figure 5.15: Power Rabi Measurement of a Global Four Qubit Dark State. Sideports driving the antisymmetric global dark state $|D_3\rangle$ with the gradient field they excite at the qubit location. The global dark state is degenerate with the global bright state $|B_4\rangle$, but it remains decoupled from the waveguide. Consequently, after each dark state driving pulse, a waveguide transmission pulse can be sent to read out the dark state population. A pulse schematic of the measurement (top right) and a linecut from the Rabi map at the resonance frequency of the global dark state at 7.325 GHz. In this measurement, the global dark state is driven exclusively by one sideport, although it should be feasible to drive it using both sideports simultaneously. When driven by a single sideport, the contrast is reduced because the bright state is also affected by the drive pulse.

we could not run the measurement for long time and with many averages, resulting in a relatively noisy background level to which the measurement decays.

To further analyze noise susceptibility, we perform the Hahn-Echo sequence to determine the T_2 -echo time. The measurement procedure closely resembles the previous case: we initiate the system by applying a $\pi/2$ -pulse, creating a superposition state. After an initial excitation pulse, we allow the system to evolve freely. Then, we apply a π inversion pulse to refocus any inhomogeneous dephasing. After another waiting interval, the final $\pi/2$ -pulse is sent through the sideport to return the system to its ground state. Immediately afterward, we perform a readout on the bright state $|B_4\rangle$ using the waveguide. The resulting echo signal reveals the coherence decay, providing insights into the relaxation properties of the system. Figure 5.18 displays the measurement data, which we fit with an exponentially decaying function 5.1 to extract the dephasing parameter $T_2^e \approx 1\mu\text{m}$. The Hahn echo T_2 characterizes both the dephasing effects and other relaxation processes, unlike the T_2^* which can be referred to as "pure dephasing" [35]. Due to the refocusing π -pulse, we

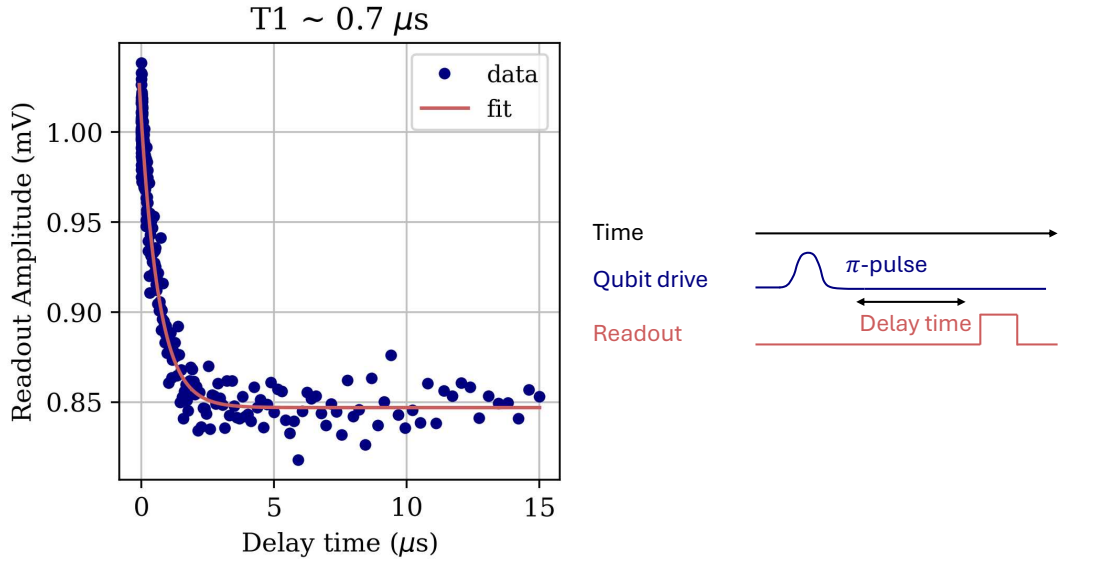


Figure 5.16: The Relaxation Time T_1 of the Global Dark State. The data is fitted with an exponential decaying function to extract the T_1 parameter. A Gaussian π -pulse is sent through the sideport to excite the dark state transition with subsequent readout measurement through the waveguide, schematically sketched on the right.

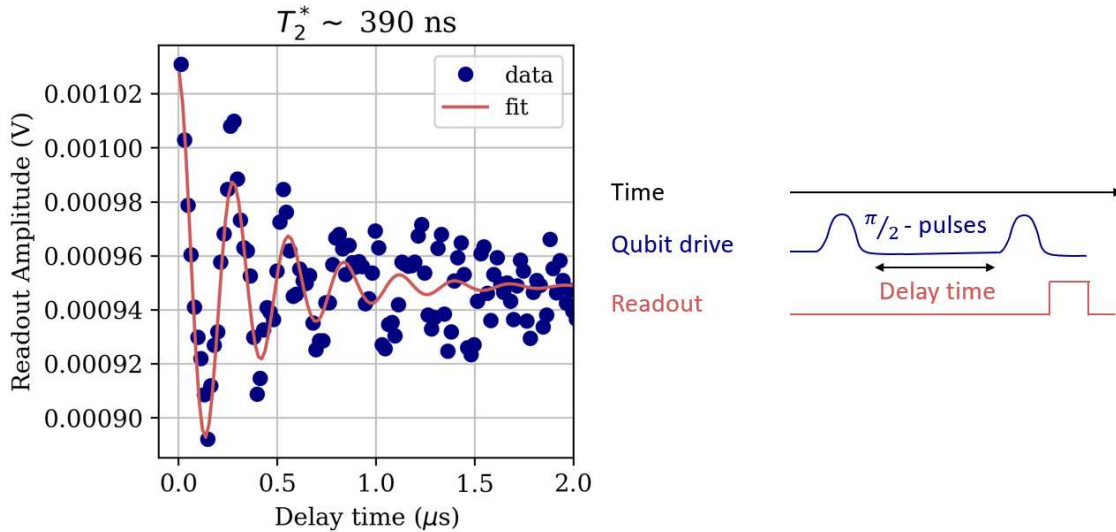


Figure 5.17: The Dephasing Time of the Global Dark State. The dephasing time T_2^* , can be extracted by fitting the data obtained from the Ramsey measurement scheme to an exponentially decaying sine function described by eq. 5.2. The T_2^* parameter has a fit error of $6.27 \cdot 10^{-9}$.

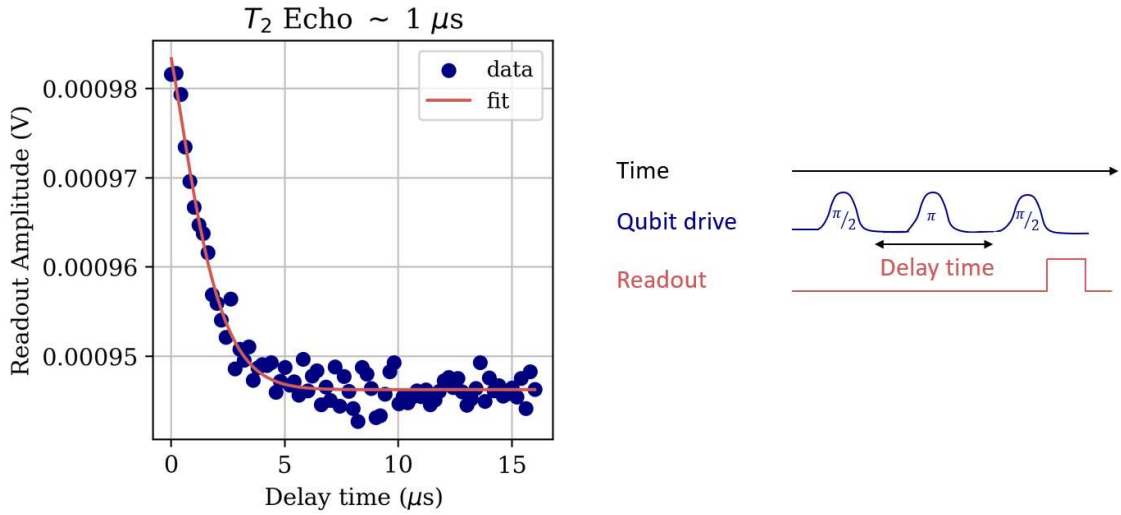


Figure 5.18: Dephasing Hahn Echo Time of the Global Dark State. A $\pi/2$ -pulse is sent via the sideport to bring the state to a superposition state, followed by refocusing π -pulse while the system is evolving freely. Another $\pi/2$ -pulse brings the system back to the ground state and waveguide transmission measurement reveals the dark state population. The fitted parameter T_2^e has a fit error of $5.98 \cdot 10^{-8}$.

expect the Echo dephasing time to be longer than T_2^* . The maximal contrast in this measurement is reduced compared to Figure 5.17. We attribute this decrease to frequency hopping of the state caused by external magnetic field fluctuations, which impacts the drive amplitudes corresponding to π - and $\pi/2$ -pulses. The entire measurement process spanned approximately an hour.

Conclusions and Outlook

Implementing a four-transmon experiment is the first step in advancing waveguide QED as a platform to investigate many-body interactions in 3D. In this thesis I have characterized an experimental system consisting of a four transmon qubits strongly coupled to an open environment - the waveguide. Waveguide mediates interactions between the qubits and can be used to read out the qubit internal degrees of freedom coupled to the waveguide propagating modes. Direct capacitive coupling between two resonant transmons gives rise to manifold of collective states, with a strongly waveguide-coupled bright state $|B_{1,2}\rangle$ and completely decoupled dark state $|D_{1,2}\rangle$, which has decoherence rate only limited by non-radiative decay. For the local dark state, we have measured the best relaxation time of $26\mu\text{m}$, which demonstrates effective protection against the decay into the waveguide. A complete experimental system with four transmon qubits possesses a dark state localized at the position of each qubit pair and two global dislocalized states in one-excitation manifold - the global dark state and global bright state. After developing and optimizing a flux-tuning scheme, we demonstrated the common- and differential tuning modes, using which we have brought both transmon pairs into resonance and used waveguide-mediated interactions to decouple a dislocalized dark state $|D_3\rangle$ and global bright state $|B_4\rangle$. By sending excitations through the sideport we achieve a coherent control of the anti-symmetric dark state and read out its population via waveguide transmission measurements of the global bright state.

This experiment is a follow-up experiment of [60], where we have used an adiabatic elimination scheme realized by waveguide coupling γ_r that is so strong, that we eliminate population leakage from $|D_3\rangle$ to the higher-excitation state $|B_{14}\rangle$ [53]. In the next steps, we need to establish a better control of the multi-qubit dark state utilizing both sideports simultaneously and optimizing the phase difference between the sideport drives. With better control and with strong waveguide coupling we aim to realize dark-state two-qubit gates by creating a chain of four qubits [46]. The computational subspace would be spanned by the two local dark states and applying a 2π -pulse from the ground state to the global dark state $|D_3\rangle$ would introduce a conditional phase shift, enabling the implementation of a CPhase gate. In the future, multi-qubit dark states in waveguide QED could become a promising platform for studying the dynamics of quantum many-body interactions [2, 25], investigating many-body localization in disordered arrays [20, 43] or even as a platform for quantum simulations of open systems taking advantage of the strong waveguide coupling and decoherence-free subspaces given by the dark states [46]. Taking the two-excitation manifold into account to transfer the information to itinerant waveguide photons opens the door to creation of qubit cluster states [7] coupled to the propagating modes in the waveguide, to study the entanglement between photons at different frequencies. A copla-

nar 2D waveguide chip design is being currently implemented in our research group, for easier scalability of the qubit chain, setting another building block to development of this exciting quantum computing approach.

Bibliography

- [1] 40 years of quantum computing. *Nature Reviews Physics*, 4(1):1–1, jan 2022. doi: 10.1038/s42254-021-00410-6.
- [2] Andreas Albrecht, Loïc Henriët, Ana Asenjo-Garcia, Paul B Dieterle, Oskar Painter, and Darrick E Chang. Subradiant states of quantum bits coupled to a one-dimensional waveguide. *New Journal of Physics*, 21(2):025003, February 2019. ISSN 1367-2630. doi: 10.1088/1367-2630/ab0134.
- [3] Ehud Altman, Kenneth R Brown, Giuseppe Carleo, Lincoln D Carr, Eugene Demler, Cheng Chin, Brian DeMarco, Sophia E Economou, Mark A Eriksson, Kai-Mei C Fu, et al. Quantum simulators: Architectures and opportunities. *PRX quantum*, 2(1):017003, 2021.
- [4] O. Astafiev, A. M. Zagoskin, A. A. Abdumalikov, Yu. A. Pashkin, T. Yamamoto, K. Inomata, Y. Nakamura, and J. S. Tsai. Resonance fluorescence of a single artificial atom. *Science*, 327(5967):840–843, February 2010. ISSN 1095-9203. doi: 10.1126/science.1181918.
- [5] J. Bardeen, L. N. Cooper, and J. R. Schrieffer. Theory of superconductivity. *Physical Review*, 108(5):1175–1204, December 1957. ISSN 0031-899X. doi: 10.1103/physrev.108.1175.
- [6] Charles H Bennett, Gilles Brassard, and Artur K Ekert. Quantum cryptography. *Scientific American*, 267(4):50–57, 1992.
- [7] Jean-Claude Besse, Kevin Reuer, Michele C. Collodo, Arne Wulff, Lucien Wernli, Adrian Copetudo, Daniel Malz, Paul Magnard, Abdulkadir Akin, Mihai Gabureac, Graham J. Norris, J. Ignacio Cirac, Andreas Wallraff, and Christopher Eichler. Realizing a deterministic source of multipartite-entangled photonic qubits. *Nature Communications*, 11(1), September 2020. ISSN 2041-1723. doi: 10.1038/s41467-020-18635-x.
- [8] Alexandre Blais, Arne L. Grimsmo, S.M. Girvin, and Andreas Wallraff. Circuit quantum electrodynamics. *Reviews of Modern Physics*, 93(2):025005, May 2021. ISSN 1539-0756. doi: 10.1103/revmodphys.93.025005.
- [9] Sergey Bravyi, Oliver Dial, Jay M. Gambetta, Dario Gil, and Zaira Nazario. The future of quantum computing with superconducting qubits. *Journal of Applied Physics*, 132(16), oct 2022. doi: 10.1063/5.0082975.
- [10] Tommaso Caneva, Marco T Manzoni, Tao Shi, James S Douglas, J Ignacio Cirac, and Darrick E Chang. Quantum dynamics of propagating photons with strong interac-

- tions: a generalized input–output formalism. *New Journal of Physics*, 17(11):113001, October 2015. ISSN 1367-2630. doi: 10.1088/1367-2630/17/11/113001.
- [11] Qi-Ming Chen, Matti Partanen, Florian Fesquet, Kedar E. Honasoge, Fabian Kronowetter, Yuki Nojiri, Michael Renger, Kirill G. Fedorov, Achim Marx, Frank Deppe, and Rudolf Gross. Scattering coefficients of superconducting microwave resonators. ii. system-bath approach. *Physical Review B*, 106(21):214506, December 2022. ISSN 2469-9969. doi: 10.1103/physrevb.106.214506.
- [12] Qi-Ming Chen, Meike Pfeiffer, Matti Partanen, Florian Fesquet, Kedar E. Honasoge, Fabian Kronowetter, Yuki Nojiri, Michael Renger, Kirill G. Fedorov, Achim Marx, Frank Deppe, and Rudolf Gross. Scattering coefficients of superconducting microwave resonators. i. transfer matrix approach. *Physical Review B*, 106(21):214505, December 2022. ISSN 2469-9969. doi: 10.1103/physrevb.106.214505.
- [13] Claude Cohen-Tannoudji, Bernard Diu, and Franck Laloë. *Quantum Mechanics, Volume 1*. Wiley, 1977. ISBN 978-0471164333.
- [14] M. J. Collett and C. W. Gardiner. Squeezing of intracavity and traveling-wave light fields produced in parametric amplification. *Physical Review A*, 30(3):1386–1391, September 1984. ISSN 0556-2791. doi: 10.1103/physreva.30.1386.
- [15] Andrew J Daley, Immanuel Bloch, Christian Kokail, Stuart Flannigan, Natalie Pearson, Matthias Troyer, and Peter Zoller. Practical quantum advantage in quantum simulation. *Nature*, 607(7920):667–676, 2022.
- [16] M. Dalmonte, S. I. Mirzaei, P. R. Muppalla, D. Marcos, P. Zoller, and G. Kirchmair. Realizing dipolar spin models with arrays of superconducting qubits. *Physical Review B*, 92(17):174507, November 2015. ISSN 1550-235X. doi: 10.1103/physrevb.92.174507.
- [17] Michel H Devoret, Benjamin Huard, Robert Schoelkopf, and Leticia F Cugliandolo. *Quantum machines: measurement and control of engineered quantum systems*, volume 96. Oxford University Press, USA, 2014.
- [18] F. Arute et al. Quantum supremacy using a programmable superconducting processor. *Nature*, 574(7779):505–510, oct 2019. doi: 10.1038/s41586-019-1666-5.
- [19] Shanhui Fan, Şükrü Ekin Kocabaş, and Jung-Tsung Shen. Input-output formalism for few-photon transport in one-dimensional nanophotonic waveguides coupled to a qubit. *Physical Review A*, 82(6):063821, December 2010. ISSN 1094-1622. doi: 10.1103/physreva.82.063821.
- [20] N. Fayard, L. Henriët, A. Asenjo-Garcia, and D. E. Chang. Many-body localization in waveguide quantum electrodynamics. *Physical Review Research*, 3(3):033233, September 2021. ISSN 2643-1564. doi: 10.1103/physrevresearch.3.033233.
- [21] Yvonne Y. Gao, M. Adriaan Rol, Steven Touzard, and Chen Wang. Practical guide for building superconducting quantum devices. *PRX Quantum*, 2(4):040202, November

2021. ISSN 2691-3399. doi: 10.1103/prxquantum.2.040202.
- [22] Juan José García Ripoll. *Quantum Information and Quantum Optics with Superconducting Circuits*. Cambridge University Press, July 2022. ISBN 9781107172913. doi: 10.1017/9781316779460.
- [23] Nicolas Gisin and Rob Thew. Quantum communication. *Nature photonics*, 1(3): 165–171, 2007.
- [24] A. Goban, C.-L. Hung, J.D. Hood, S.-P. Yu, J.A. Muniz, O. Painter, and H.J. Kimble. Superradiance for atoms trapped along a photonic crystal waveguide. *Physical Review Letters*, 115(6):063601, August 2015. ISSN 1079-7114. doi: 10.1103/physrevlett.115.063601.
- [25] A. González-Tudela, V. Paulisch, D.E. Chang, H.J. Kimble, and J.I. Cirac. Deterministic generation of arbitrary photonic states assisted by dissipation. *Physical Review Letters*, 115(16):163603, October 2015. ISSN 1079-7114. doi: 10.1103/physrevlett.115.163603.
- [26] Xiu Gu, Anton Frisk Kockum, Adam Miranowicz, Yu-xi Liu, and Franco Nori. Microwave photonics with superconducting quantum circuits. *Physics Reports*, 718–719: 1–102, November 2017. ISSN 0370-1573. doi: 10.1016/j.physrep.2017.10.002.
- [27] O. Dial J. Chow and J. Gambetta. Ibm quantum breaks the 100-qubit processor barrier. *IBM Research Blog*, 2021. URL <https://research.ibm.com/blog/127-qubit-quantum-processor-eagle>.
- [28] X.Y. Jin, A. Kamal, A.P. Sears, T. Gudmundsen, D. Hover, J. Miloshi, R. Slattery, F. Yan, J. Yoder, T.P. Orlando, S. Gustavsson, and W.D. Oliver. Thermal and residual excited-state population in a 3d transmon qubit. *Physical Review Letters*, 114(24): 240501, June 2015. ISSN 1079-7114. doi: 10.1103/physrevlett.114.240501.
- [29] J.R. Johansson, P.D. Nation, and Franco Nori. Qutip 2: A python framework for the dynamics of open quantum systems. *Computer Physics Communications*, 184(4): 1234–1240, April 2013. ISSN 0010-4655. doi: 10.1016/j.cpc.2012.11.019.
- [30] B.D. Josephson. Possible new effects in superconductive tunnelling. *Physics Letters*, 1(7):251–253, jul 1962. doi: 10.1016/0031-9163(62)91369-0.
- [31] Bharath Kannan. *Waveguide quantum electrodynamics with superconducting qubits*. PhD thesis, Massachusetts Institute of Technology, 2018.
- [32] M. S. Khalil, M. J. A. Stoutimore, F. C. Wellstood, and K. D. Osborn. An analysis method for asymmetric resonator transmission applied to superconducting devices. *Journal of Applied Physics*, 111(5), March 2012. ISSN 1089-7550. doi: 10.1063/1.3692073.

- [33] Morten Kjaergaard, Mollie E. Schwartz, Jochen Braumüller, Philip Krantz, Joel I.-J. Wang, Simon Gustavsson, and William D. Oliver. Superconducting qubits: Current state of play. *Annual Review of Condensed Matter Physics*, 11(1):369–395, mar 2020. doi: 10.1146/annurev-conmatphys-031119-050605.
- [34] Jens Koch, Terri M. Yu, Jay Gambetta, A. A. Houck, D. I. Schuster, J. Majer, Alexandre Blais, M. H. Devoret, S. M. Girvin, and R. J. Schoelkopf. Charge-insensitive qubit design derived from the cooper pair box. *Physical Review A*, 76(4):042319, oct 2007. doi: 10.1103/physreva.76.042319.
- [35] P. Krantz, M. Kjaergaard, F. Yan, T. P. Orlando, S. Gustavsson, and W. D. Oliver. A quantum engineers guide to superconducting qubits. *Applied Physics Reviews*, 6(2), jun 2019. doi: 10.1063/1.5089550.
- [36] Philipp Kurpiers, Theodore Walter, Paul Magnard, Yves Salathe, and Andreas Wallraff. Characterizing the attenuation of coaxial and rectangular microwave-frequency waveguides at cryogenic temperatures. *EPJ Quantum Technology*, 4(1), May 2017. ISSN 2196-0763. doi: 10.1140/epjqt/s40507-017-0059-7.
- [37] Kevin Lalumière, Barry C. Sanders, A. F. van Loo, A. Fedorov, A. Wallraff, and A. Blais. Input-output theory for waveguide qed with an ensemble of inhomogeneous atoms. *Physical Review A*, 88(4):043806, October 2013. ISSN 1094-1622. doi: 10.1103/physreva.88.043806.
- [38] Nathan Marcuvitz. *Waveguide handbook*. Number 21. Iet, 1951.
- [39] Mohammad Mirhosseini, Eunjong Kim, Xueyue Zhang, Alp Sipahigil, Paul B. Dieterle, Andrew J. Keller, Ana Asenjo-Garcia, Darrick E. Chang, and Oskar Painter. Cavity quantum electrodynamics with atom-like mirrors. *Nature*, 569(7758):692–697, May 2019. ISSN 1476-4687. doi: 10.1038/s41586-019-1196-1.
- [40] William J Munro, Ashley M Stephens, Simon J Devitt, Keith A Harrison, and Kae Nemoto. Quantum communication without the necessity of quantum memories. *Nature Photonics*, 6(11):777–781, 2012.
- [41] Mahdi Naghiloo. Introduction to experimental quantum measurement with superconducting qubits. *arXiv preprint arXiv:1904.09291*, 2019.
- [42] Jeremy L O’Brien. Optical quantum computing. *Science*, 318(5856):1567–1570, 2007.
- [43] Tuure Orell, Alexios A. Michailidis, Maksym Serbyn, and Matti Silveri. Probing the many-body localization phase transition with superconducting circuits. *Physical Review B*, 100(13):134504, October 2019. ISSN 2469-9969. doi: 10.1103/physrevb.100.134504.
- [44] Tuure Orell, Maximilian Zanner, Mathieu L. Juan, Aleksei Sharafiev, Romain Albert, Stefan Oleschko, Gerhard Kirchmair, and Matti Silveri. Collective bosonic effects in

- an array of transmon devices. *Physical Review A*, 105(6):063701, June 2022. ISSN 2469-9934. doi: 10.1103/physreva.105.063701.
- [45] Alexandre Paquette, Joël Griesmar, Gabriel Lavoie, Romain Albert, Florian Blanchet, Alexander Grimm, Ulrich Martel, and Max Hofheinz. Absorptive filters for quantum circuits: Efficient fabrication and cryogenic power handling. *Applied Physics Letters*, 121(12), September 2022. ISSN 1077-3118. doi: 10.1063/5.0114887.
- [46] V Paulisch, H J Kimble, and A González-Tudela. Universal quantum computation in waveguide qed using decoherence free subspaces. *New Journal of Physics*, 18(4): 043041, April 2016. ISSN 1367-2630. doi: 10.1088/1367-2630/18/4/043041.
- [47] B Peropadre, J Lindkvist, I-C Hoi, C M Wilson, J J Garcia-Ripoll, P Delsing, and G Johansson. Scattering of coherent states on a single artificial atom. *New Journal of Physics*, 15(3):035009, March 2013. ISSN 1367-2630. doi: 10.1088/1367-2630/15/3/035009.
- [48] Stefano Pirandola, Ulrik L Andersen, Leonardo Banchi, Mario Berta, Darius Bunandar, Roger Colbeck, Dirk Englund, Tobias Gehring, Cosmo Lupo, Carlo Ottaviani, et al. Advances in quantum cryptography. *Advances in optics and photonics*, 12(4): 1012–1236, 2020.
- [49] I. M. Pop, T. Fournier, T. Crozes, F. Lecocq, I. Matei, B. Pannetier, O. Buisson, and W. Guichard. Fabrication of stable and reproducible submicron tunnel junctions. *Journal of Vacuum Science amp; Technology B, Nanotechnology and Microelectronics: Materials, Processing, Measurement, and Phenomena*, 30(1), January 2012. ISSN 2166-2754. doi: 10.1116/1.3673790.
- [50] David M Pozar. *Microwave engineering: theory and techniques*. John wiley & sons, 2021.
- [51] S. Probst, F. B. Song, P. A. Bushev, A. V. Ustinov, and M. Weides. Efficient and robust analysis of complex scattering data under noise in microwave resonators. *Review of Scientific Instruments*, 86(2), February 2015. ISSN 1089-7623. doi: 10.1063/1.4907935.
- [52] S.E. Rasmussen, K.S. Christensen, S.P. Pedersen, L.B. Kristensen, T. Bækkegaard, N.J.S. Loft, and N.T. Zinner. Superconducting circuit companion—an introduction with worked examples. *PRX Quantum*, 2(4):040204, December 2021. ISSN 2691-3399. doi: 10.1103/prxquantum.2.040204.
- [53] Florentin Reiter and Anders S. Sørensen. Effective operator formalism for open quantum systems. *Physical Review A*, 85(3):032111, March 2012. ISSN 1094-1622. doi: 10.1103/physreva.85.032111.
- [54] Guillermo Romero, Juan José García-Ripoll, and Enrique Solano. Photodetection of propagating quantum microwaves in circuit qed. *Physica Scripta*, T137:014004, December 2009. ISSN 1402-4896. doi: 10.1088/0031-8949/2009/t137/014004.

-
- [55] Daniel D Stancil and Gregory T Byrd. *Principles of superconducting quantum computers*. John Wiley & Sons, 2022.
- [56] M. Tinkham. “*Introduction to Superconductivity*”, 2nd ed. Dover Publications Inc., New York,, 2004.
- [57] Arjan F. van Loo, Arkady Fedorov, Kevin Lalumière, Barry C. Sanders, Alexandre Blais, and Andreas Wallraff. Photon-mediated interactions between distant artificial atoms. *Science*, 342(6165):1494–1496, December 2013. ISSN 1095-9203. doi: 10.1126/science.1244324.
- [58] Uri Vool and Michel Devoret. Introduction to quantum electromagnetic circuits. *International Journal of Circuit Theory and Applications*, 45(7):897–934, jun 2017. doi: 10.1002/cta.2359.
- [59] A. Wallraff, D. I. Schuster, A. Blais, L. Frunzio, R.-S. Huang, J. Majer, S. Kumar, S. M. Girvin, and R. J. Schoelkopf. Strong coupling of a single photon to a superconducting qubit using circuit quantum electrodynamics. *Nature*, 431(7005):162–167, September 2004. ISSN 1476-4687. doi: 10.1038/nature02851.
- [60] Maximilian Zanner. *Coherent Control of Multi-Qubit Dark States in Waveguide Quantum Electrodynamics*. phdthesis, University of Innsbruck, 2022. URL https://iqoqi.at/_groups/images/group/gk/phd_theses/phd_zanner.pdf.
- [61] Han-Sen Zhong, Hui Wang, Yu-Hao Deng, Ming-Cheng Chen, Li-Chao Peng, Yi-Han Luo, Jian Qin, Dian Wu, Xing Ding, Yi Hu, Peng Hu, Xiao-Yan Yang, Wei-Jun Zhang, Hao Li, Yuxuan Li, Xiao Jiang, Lin Gan, Guangwen Yang, Lixing You, Zhen Wang, Li Li, Nai-Le Liu, Chao-Yang Lu, and Jian-Wei Pan. Quantum computational advantage using photons. *Science*, 370(6523):1460–1463, dec 2020. doi: 10.1126/science.abe8770.

Acknowledgements

I would like to thank my thesis supervisor **Gerhard Kirchamir**, you have served in many ways as a scientific idol to me, with your enthusiasm for science and always positive attitude. Fighting the never ending problems with the project with endless patience explaining and guiding me through my scientific journey. You have created a great research group and a working environment in which I could learn about this fascinating field and even grow as a person.

I will always be grateful to all the members of the research group for the warm welcome in the team since the first day and never hesitating to help with solving and discussing issues with my project. Namely, I would like to thank **Teresa Höniigl-Decrinis** for all the help with this project. You have joined the efforts to help me solve all the issues with the project with great drive and expertise, without which it would not be possible for me to work successfully on this project. I also thank **Desi, Christian and Julian** for creating a very friendly and productive environment in the office and always helping, as well as other members of the group such as **Ian, Vasilisa** and all others.

I would like to express my gratitude to **Max Zanner**, who was my first mentor in the group introducing me to this field and the project that has kept me busy ever since I have started working in the group. I initially joined the group as a summer student thanks to your invitation after a lab tour and it has shaped my entire master studies since.

I want to thank to my loving parents **Zuzana** and **Vladimir** for their never ending support.

And last but definitely not least I want to mention my life partner **Erja**. You were always listening to my complaints and concerns related not only to my research project and supporting me on this journey. Thank you, without you I could not handle it. I also want to thank you for your patience and effort in helping me to illustrate the figures in this thesis.